Silicon-Germanium Saturable Absorbers and Erbium-doped Waveguides for Integrated Mode-locked Lasers

by

Hyunil Byun

Submitted to the Department of Electrical Engineering and Computer Science
in partial fulfillment of the requirements for the degree of

Master of Science

at the

MASSACHUSETTS INSTITUTE OF TECHNOLOGY

May 2006
[June 2006]

Author . . . .
Department of Electrical Engineering and Computer Science
May 25, 2006

Certified by . . . .
Franz X. Kärtner
Associate Professor
upervisor

Accepted by . . . .
Arthur C. Smith
Chairman, Department Committee on Graduate Students

Silicon-Germanium Saturable Absorbers and Erbium-doped Waveguides for Integrated Mode-locked Lasers

by

Hyunil Byun

Submitted to the Department of Electrical Engineering and Computer Science
on May 25, 2006, in partial fulfillment of the
requirements for the degree of
Master of Science

Abstract

In this thesis, Silicon-Germanium (SiGe) Saturable Bragg Reflectors (SBR) and Erbium-doped waveguide chips are fabricated and characterized as crucial components for integration of a mode-locked laser on a Si-chip. The SiGe-SBR is designed to be compatible with Si-based fabrication processes for monolithic integration and to need as little saturation fluence as possible so that it can be used for higher repetition rate lasers application. The SBRs are tested experimentally inside an Erbium glass bulk laser. We also tested Erbium-doped waveguide chips fabricated by Inplane Photonics Inc. to verify that it has enough gain to function as a gain medium of an on-chip laser. These components will be important as intermediate steps before finally integrating mode-locked laser.

Thesis Supervisor: Franz X. Kärtner
Title: Professor

Acknowledgments

First I would like to thank my research advisor Professor Franz X. Kärtner for generous support and patient mentorship. He has inspired my creativity in research and stimulated my interest in this research. I express thanks to Professor Erich Ippen for helpful advice on the nonlinear characterization of the saturable absorbers. I also thank my academic advisor Professor Haeseung Lee for warm advice on my academic life.

I would like to thank the members of my research group for numerous discussions, suggestions, equipment loans, and good friendship. Especially Felix Grawert who left last summer with doctor's degree did not spare his energy on teaching me from the scratch in the lab works, basic laser theories, and administrative procedures. Jungwon Kim, senior in my high school, gave me invaluable advice not only on my research but also on my personal matters. Jeff Chen and Ömer Ilday helped me in fiber manipulations such as splicing. Andrew Benedick gave me practical insights in mechanical processing of laser components and helped me a lot with the revision of this thesis. Ariel Gordon, my office mate, always welcomed my questions on laser theories.

My research could not have happened without help from outside of my research group. Ali Motamedi in Professor Erich Ippen's group was very active and cooperative in pump probe measurement for the resonantly-coated SiGe-SBRs. Peter Rakich and Hanfei Shen offered lots of practical advice on the experimental setup for the single pass gain measurement of the waveguide chips. Muyiwa in Professor Judy Hoyt's group prepared high quality Ge/SiO_2 layers and secured a foothold for the further development of next generation SBRs. Gale Petrich was very kind in supporting SBR preparations in Professor Leslie Kolodziejski's labratory. Libby Shaw and Tim McClure in the CMSE analysis lab greatly helped in the characterization of SBR samples with the spectro photometer and FTIR machine. Jung Yoon at Lincoln lab contributed a lot in examining new fabrication scheme of SBRs by providing a great number of samples. Peter O'Brien provided high quality coatings on SBRs and made the resonant coating working.

I thank our administrative assistants Dorothy Fleisher and Donna Gale for their hidden efforts to keep the lab running smoothly. I also thank KFAS (Korea Foundation for Advanced Studies) for supporting me financially for the first year in my graduate study.

Contents

List of Figures

List of Tables

Chapter 1

Introduction

1.1 Motivation and application

The growing demand for the bandwidth of network traffic has created need for higher data rates. However, after the crash of some major telecommunication companies, there is little interest in investing large sums to build better and faster service. The solution to this situation is to build simplified and integrated systems which will greatly surpass all current cost and performance standards. One component of such systems could be the on-chip mode locked laser: from a monolithic cavity of 5cm length, it emits pulses of less than 1ps duration at 2GHz repetition rate (e.g., Fig. 1-1). There are several advantages of integrated mode-locked lasers. First, it has

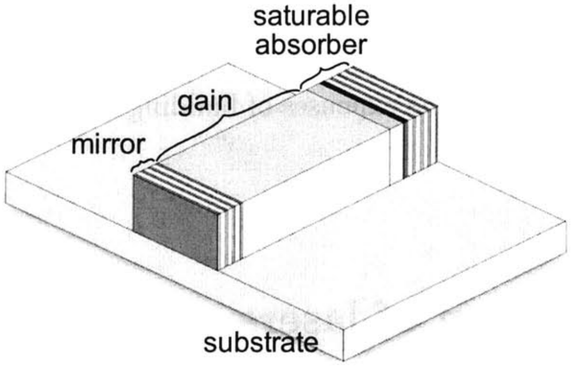

Figure 1-1: Schematic of on-chip integrated mode locked laser.

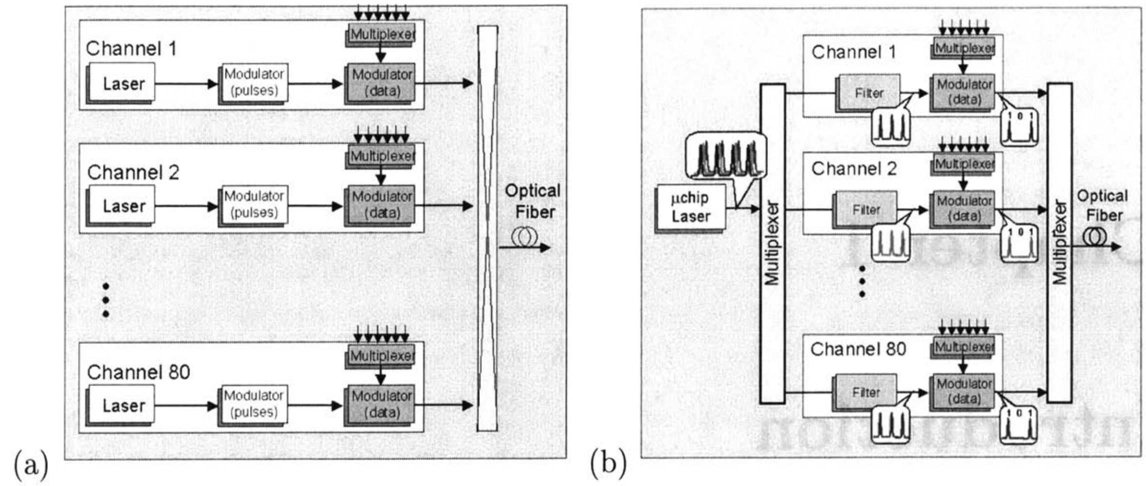

Figure 1-2: Comparison between (a) conventional communication system and (b) future system. In the future, microchip-laser can replace current discrete laser array and reduce the cost for building system [8].

much lower noise and jitter compared to electrical signal. Second, the repetition rate can be as high as several tens of GHz since the cavity length can be very small. Third, it is mass-producible, which is crucial reason for being able to cut down on the price of individual components.

In today's optical communication systems, optical signals in the C-band ranging from 1530nm to 1560nm are generally used. In Fig. 1-2 (a), a schematic of a conventional communication system is shown, where eighty discrete lasers are used to span the C-band because each laser covers only narrow bandwidth. On the contrary, an on-chip mode-locked laser that spans the whole C-band can do the job that the bundle of discrete lasers have been doing. On-chip mode-locked lasers are expected replace current lasers and cut down on the expenses of building communication systems (Fig. 1-2 (b)).

1.2 The operation of lasers

A laser is composed of three elements: gain medium which amplifies incoming light over specific wavelength ranges, pumping which excites or activates the gain medium,

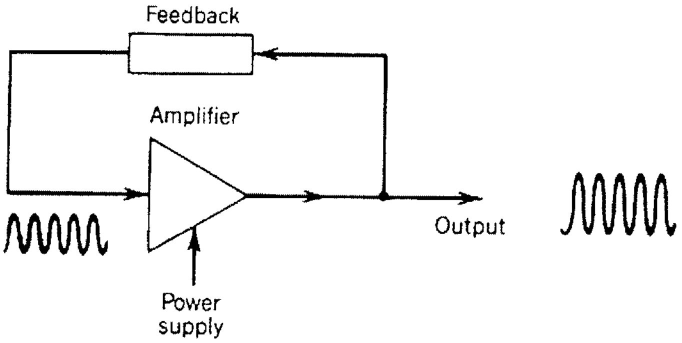

Figure 1-3: A laser can be seen as an oscillator with an amplifier and positive feedback. [3]

and resonator which provides optical feedback.

A laser can be understood as an optical analogy of an electronic oscillator consisting of an amplifier and positive feedback. In the feedback system of Fig. 1-3, a small amount of noise at the input of the amplifier undergoes amplification. The output is fed back into the input and further amplification occurs. When we assume that the gain of amplifier is greater than the loss in the feedback, this iteration could lead to infinitely large amplitude of output light, but the output amplitude is limited by the saturation of the gain medium. As larger signal is fed back, the gain is reduced. Thus a stable condition is reached when the reduced gain is equal to the loss in the whole loop.

In reality, the amplifier is the pumped active medium. Gain saturation is an intrinsic property of laser amplifiers. Larger signals bleach more of the inversion to which the gain is proportional. Feedback is obtained by placing the active medium in an optical resonator where light is reflected back and forth between two end mirrors. In order to make use of the laser light, one of the mirrors is designed to transmit small portions of the this reflecting light.

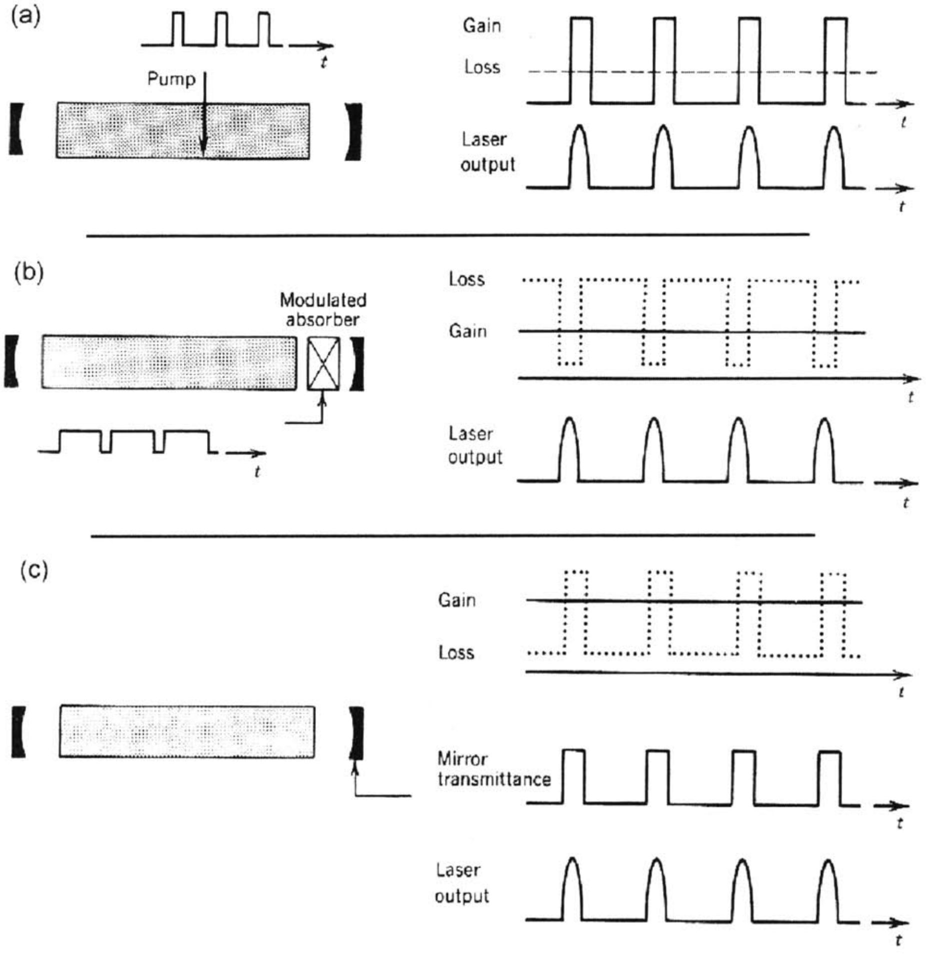

Figure 1-4: Three different methods of pulsing lasers. (a) Gain switching (b) Q-switching (c) Cavity dumping. All three methods are internally modulating the laser. [3]

1.3 Pulsed lasers and mode locking

1.3.1 Pulsed lasers

In order to get short pulse from a laser, the simplest way is to modulate the output laser with an external drive and to allow the pulse to pass during selected short time intervals. However, this external modulation has two disadvantages. First it is inefficient since the output laser is not used during being blocked. Second the peak power can never be larger than that of the continuous source.

A laser can be more efficiently pulsed by an internal modulation. There are four common methods for the internal modulation: gain switching, Q-switching, cavity dumping, and mode locking.

Gain Switching The laser pump is turned on and off to control the cavity gain. When the pump is on, the gain is larger than the overall loss and the laser light is generated. When the pump is off, no light comes out.

Q-switching The resonator loss is controlled by means of loss modulator. In order to produce laser light during a time interval, the loss of the modulator is reduced below the gain for the desired interval. Since the pump continues to deliver power to the resonator, the energy is accumulated in the form of inverse population during the off-time and it is released as soon as the loss goes below the gain.

Cavity dumping During the off-time, the mirror does not allow the intracavity power to be released, while the mirror transmits part of laser light during the on-time. In this scheme, the pump energy is stored during the off-time, so large amount of energy can be released when the mirror transmissivity suddenly increases.

Mode locking This scheme is quite different from the previous three schemes. There are many individual longitudinal modes equally spaced with $c/2L$ interval in an optical oscillator. Although these modes run independently, techniques exist to lock their phases. Then the modes look like a Fourier-series expansion of a pulse train with the period of $T_F = 2L/c$. Several ways for mode locking are shown in the following section.

Fig. 1-4 illustrates three schemes to internally modulate the laser light for pulsing.

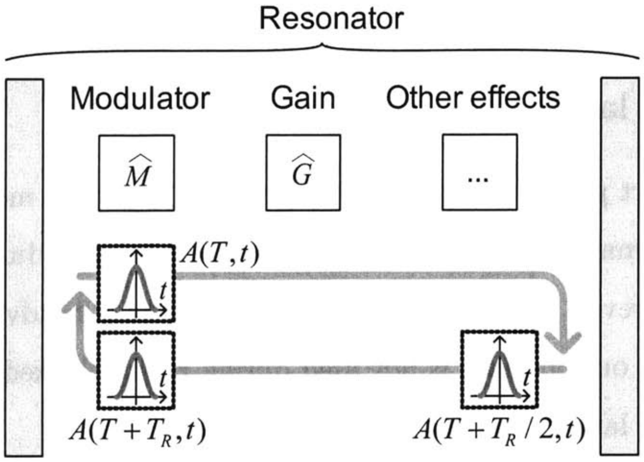

Figure 1-5: Modelling of a resonator in terms of pulse envelope and its evolution. A denotes the envelope of a pulse. T is a coarse-grained time scale on multiples of the round-trip time and t is a smaller time scale to describe the shape of the pulse referred to a specific point in the resonator.

1.3.2 Mode locking

Master equation

In order to see how a laser is mode locked, it is instructional to write the pulse evolution into equations in either time domain or frequency domain. In this subsection, a general form of the master equation describing mode locking is explored.

In Fig. 1-5 a resonator is modelled with notations to describe a pulse travelling inside. There are two different time scales, T and t. T a larger time scale to show the position of the pulse along the resonator length and t is a smaller time scale to describe the shape of the pulse at a specific position in the resonator. Envelope $A(T,t)$ evolves into $A(T+T_R,t)$ after one round trip, where T_R is round trip time. To satisfy self-consistency,

$$A(T+T_R,t) = A(T,t)\left[(1+\widehat{M})(1+\widehat{G})\cdots(1+\widehat{X})\right], \tag{1.1}$$

where $\widehat{M}$ is operator for modulator, and $\widehat{G}$ is for gain medium. Other effects can be added similarly to the modulator or the gain medium. Assuming small change per pass,

$$\begin{aligned} A(T+T_R,t) - A(T,t) &= \left[\widehat{M} + \widehat{G} + \cdots + \widehat{X}\right] \\ T_R \frac{\partial A(T,t)}{\partial T} &= \left[\widehat{M} + \widehat{G} + \cdots + \widehat{X}\right]. \end{aligned} \tag{1.2}$$

Each component is described by

$$\begin{aligned} \widehat{G} &= g(T) + D_g \tfrac{\partial^2}{\partial t^2} && \text{(Gain medium.)} \\ \widehat{C} &= -l && \text{(Cavity loss. Dispersion neglected.)} \\ \widehat{Q} &= q(T,t) && \text{(Modulated loss.).} \end{aligned} \tag{1.3}$$

The second derivative term in Eqn. 1.3 denotes the dispersion of the gain medium. The dispersion is proportional to the square of the frequency and this corresponds to the second derivative in the time domain.

Active modelocking

For active modelocking, an amplitude modulator such as an acousto-optic modulator or electro-optic modulator is used inside the cavity. The amplitude modulator changes the loss with the rate equal to the laser round-trip frequency $\omega_M = 2\pi c/2L$. The modulation introduces sidebands for every mode in the frequency domain. A mode centered at ω_0 will obtain two sidebands at $\omega_0 \pm \omega_M$. If we make sure that ω_M is the mode spacing, each mode competes for gain with adjacent modes and the most efficient operation is achieved when the phase of each mode is locked to each other.

The master equation is given by [16]

$$T_R \frac{\partial A(T,t)}{\partial T} = \left[g(T) + D_g \frac{\partial^2}{\partial t^2} - l - M(1-\cos(\omega_M t))\right] A(T,t), \tag{1.4}$$

where gain, cavity loss and modulated loss are included. The term $M(1-\cos(\omega_M t))$ corresponds to the modulated loss $q(t)$. Near the minimum points of loss, the pulse is generated and the cosine function can be approximated by a parabola: $1-\cos(\omega_M t) \simeq M_s t^2$, where $M_s = M\omega_M^2/2$. Then Eqn. 1.4 reduces to

$$T_R \frac{\partial A(T,t)}{\partial T} = \left[g - l + D_g \frac{\partial^2}{\partial t^2} - M_s t^2\right] A(T,t). \tag{1.5}$$

Eqn. 1.5 is known to have the Hermite-Gaussian solutions

$$A_n(T,t) = A_n(t)e^{\lambda_n T/T_R}, \tag{1.6}$$

$$A_n(t) = C_n H_n(t/\tau_a)e^{-t^2/2\tau_a^2}, \tag{1.7}$$

where λ_n is the eigenvalue, C_n is a mode dependent constant, and τ_a defines the width of the Gaussian, which is given by

$$\tau_a = \sqrt[4]{D_g/M_s}. \tag{1.8}$$

Passive modelocking

While it is relatively simple to design and implement, active mode locking has several limitations. One of the major disadvantages of active modelocking is that the pulse width scales with the fourth root of the modulation strength M_s. The pulse width is also not very sensitive to the modulation strength and it is hard to scale the pulse width down by increasing the modulation strength. In addition, actively mode locked lasers are usually not able to take advantage of the available bandwidth of the gain medium. There are obvious limitations to the speed of the modulation, ω_M, since electrical signals are involved. Because of these limitations, passive mode locking is usually implemented in applications where high repetition rates and short pulses are required.

In passive modelocking a device with intensity-dependent loss is placed in the cavity. If the loss decreases with intensity, pulse formation is favored. True saturable absorber, colliding pulse modelocking, or Kerr lens modelocking can be applied to provide the desired intensity-loss relation. Passive mode locking generates much shorter pulses than active mode locking does since the pulse inside the laser self-modulates itself, more rapidly than would be possible with any active modulation. [12]

Based on the ratio between the recovery time of the saturable absorber and the width of generated pulse, a saturable absorber can be categorized into a fast saturable absorber or slow saturable absorber. Slow saturable absorbers respond to the fluence of the pulse or the integration of intensity over the pulse period. For a slow saturable absorber, the recovery time is much longer than the pulse duration, but it should be smaller than the cavity round trip time so that the absorber is fully recovered between two consecutive pulses. Most of the semiconductor saturable absorbers are slow saturable absorber for sub-picosecond pulses. The opposite case is the fast saturable absorber which responds immediately to the pulse intensity. The recovery time of a fast saturable absorber is much smaller than the pulse duration.

The work in this thesis is centered around the dynamics of passively mode-locked lasers by semiconductor absorbers. Their master equation is given by

$$\begin{aligned} T_R \frac{\partial A(T,t)}{\partial T} &= \left[g(t) - q(t) - l + D_f \frac{\partial^2}{\partial t^2} \right] A(T,t) \qquad (1.9) \\ \text{with} \quad g(t) &= g \text{ and} \\ q(t) &= \frac{q_0}{1 + \frac{|A(T,t)|^2}{P_A}} \simeq q_0 \left(1 - \frac{|A(T,t)|^2}{P_A}\right) \text{ for nonsaturated case} \end{aligned}$$

where g is the initial small signal gain of the medium just before the pulse arrives (in other words, the gain saturated by the average power), $q(t)$ is the loss of the saturable absorber, E_L is the saturation energy of the gain, and P_A is the saturation power of the absorber. The loss of the absorber immediately responds to the pulse power and the gain is assumed not to be saturated by a single pulse. The solution of Eqn. 1.9 is known to be of the form $A(t) = A_0 \mathrm{sech}(t/\tau)$, where τ is the pulse width. [16]

Q-switching instability

A solid-state laser passively mode-locked by a saturable absorber can be plagued by Q-switched mode locking (QML). In this regime, the pulse energy changes along a Q-switched envelop (Fig. 1-6). The Q-switching instabilities are usually unwanted for applications where constant pulse energies and high repetition rates are required.

When using semiconductor saturable absorber mirrors (SESAM's), one criterion to guarantee cw mode locking against QML is to have pulse energies higher than the threshold given by

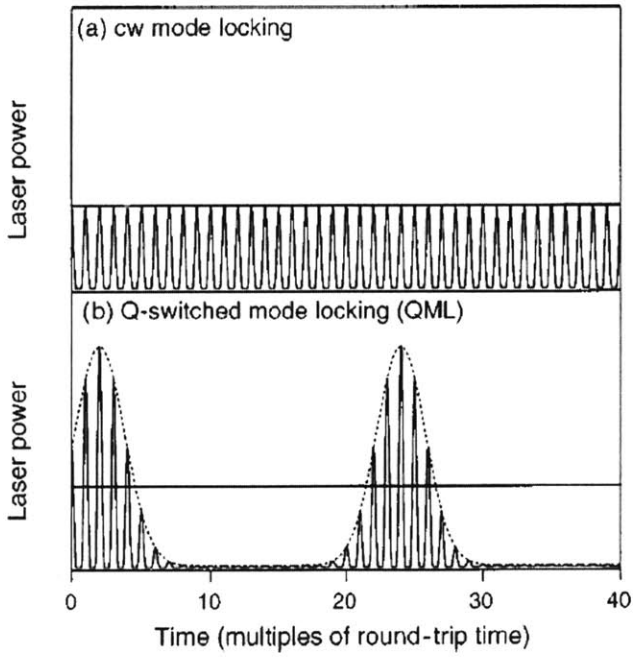

Figure 1-6: Laser power versus time for (a) a stable cw mode-locked laser and for (b) a Q-switched mode-locked laser

$$\begin{aligned} E_{P,c} &\equiv (E_{sat,L} E_{sat,A} \Delta R)^{1/2} \\ &= (F_{sat,L} A_{eff,L} F_{sat,A} A_{eff,A} \Delta R)^{1/2}, \end{aligned} \tag{1.10}$$

where $F_{sat,L}$ is the saturation fluence of the gain, $A_{eff,L}$ is the effective mode area in the gain, $F_{sat,A}$ is the saturation fluence of the absorber, $A_{eff,A}$ is the spot area on the absorber, and ΔR is the modulation depth of the absorber. In other words, the pulse energy $E_P > E_{P,c}$ is required to obtain stable cw mode locking.

The physics of this relation can be understood as follows. If the pulse energy rises slightly by noise fluctuations of the laser, this pulse energy first grows exponentially because the absorber is saturated more strongly and the cavity loss decreases. If this rise is not balanced by a stronger saturation of the gain, then the pulse energy will increase further and self Q-switching starts. The laser is stable against QML if the gain saturation is sufficiently strong to stop the exponential rise. Since the gain saturation gets stronger for higher energy pulse, the pulse energy should be high enough to saturate the gain and to suppress the fluctuations. [18, 5]

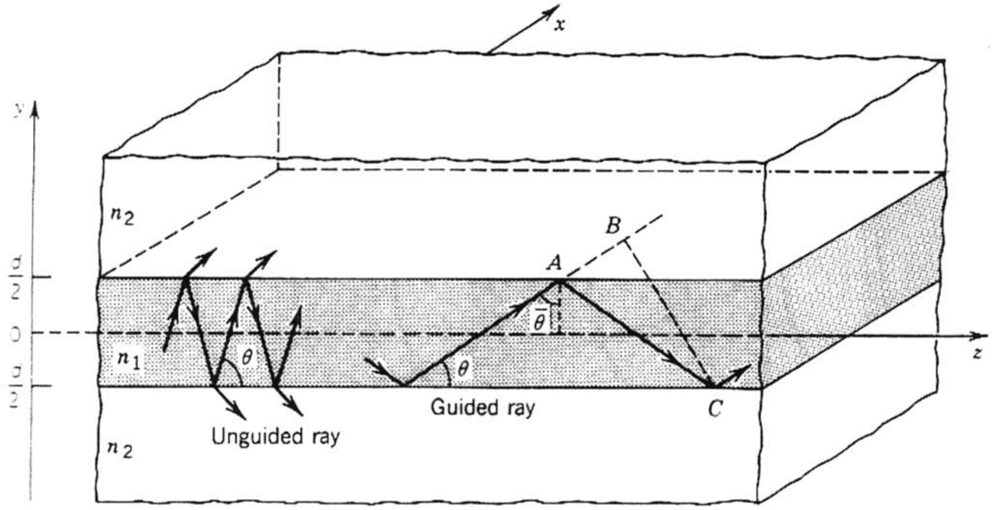

Figure 1-7: Planar dielectric waveguide. Rays making an angle $\theta < \overline{\theta}_c = \cos^{-1}(n_2/n_1)$ are guided by total internal reflection. [3]

1.4 Waveguide optics

An optical waveguide can be an efficient way to transmit optical waves. It is a light conduit consisting of a slab, strip, or cylinder or dielectric material surrounded by another dielectric material of lower refractive index. Dielectric waveguides can be relatively easily integrated into a chip and may connect the integrated optical components to each other. In face, if a dielectric waveguide can be doped with proper material, it can serve not only as a waveguide, but as a gain medium for a laser. In this section, we focus on explaining the basic theory of dielectric waveguides.

1.4.1 Planar dielectric waveguides

Fig. 1-7 illustrates a planar dielectric waveguide where a slab of thickness d and refractive index n_2 is surrounded by a cladding of smaller refractive index n_1. If an optical wave incident with an angle smaller than $\overline{\theta}_c = \cos^{-1}(n_2/n_1)$, it can be guided by total internal reflection.

Allowed modes are determined by requiring self-consistency condition that an optical wave reproduces itself after reflecting twice. In other words, for each mode, the phase shift between the two waves should be multiple of 2π,

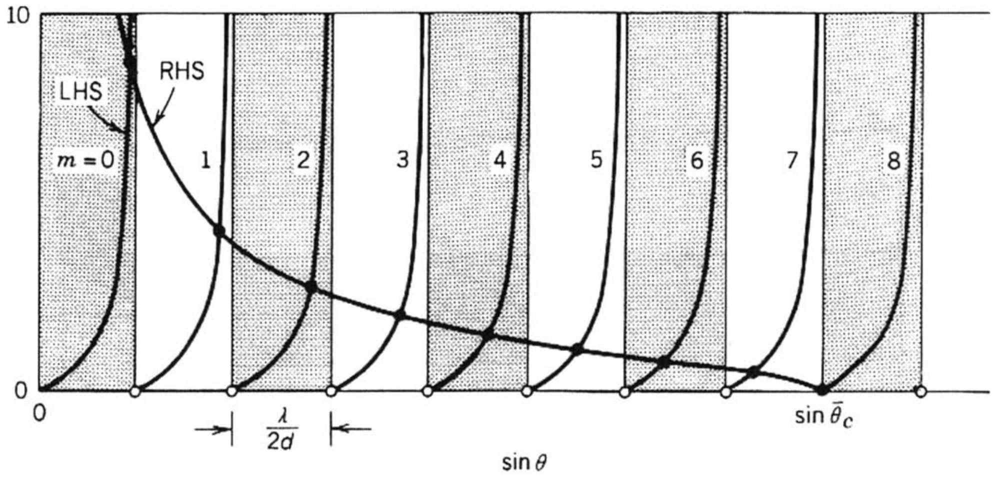

Figure 1-8: Graphical solution of self-consistency condition to determine the bounce angle θ_m of the modes of a dielectric waveguide. [3]

$$\frac{2\pi}{\lambda}2d\sin\theta - 2\varphi_r = 2\pi m, \quad m = 0, 1, 2, ... \tag{1.11}$$

where φ_r is the phase shift introduced by dielectric interface and in the TE case it is given by

$$\tan\frac{\varphi}{2} = \left(\frac{\sin^2\overline{\theta}_c}{\sin^2\theta} - 1\right)^{1/2} \tag{1.12}$$

Rewriting 1.11 and 1.12, we obtain

$$\tan\left(\pi\frac{d}{\lambda}\sin\theta - m\frac{\pi}{2}\right) = \left(\frac{\sin^2\overline{\theta}_c}{\sin^2\theta} - 1\right)^{1/2} \tag{1.13}$$

Fig. 1-8 plots the graphs of left-hand-side and right-hand-side of Eqn. 1.13 to solve it for $\sin\theta$. In case of Fig. 1-8, there are nine solutions from $m = 0$ to $m = 8$ which correspond to nine modes with bound angle of θ_m. Then the propagation constants along the slab are

$$\beta_m = n_1 k_0 \cos\theta_m \tag{1.14}$$

From Fig. 1-8, we can note that there is one solution in each segment of $\frac{\lambda}{2d}$ along $\sin\theta$ axis. The filled circles mark each solution. The number of modes can be

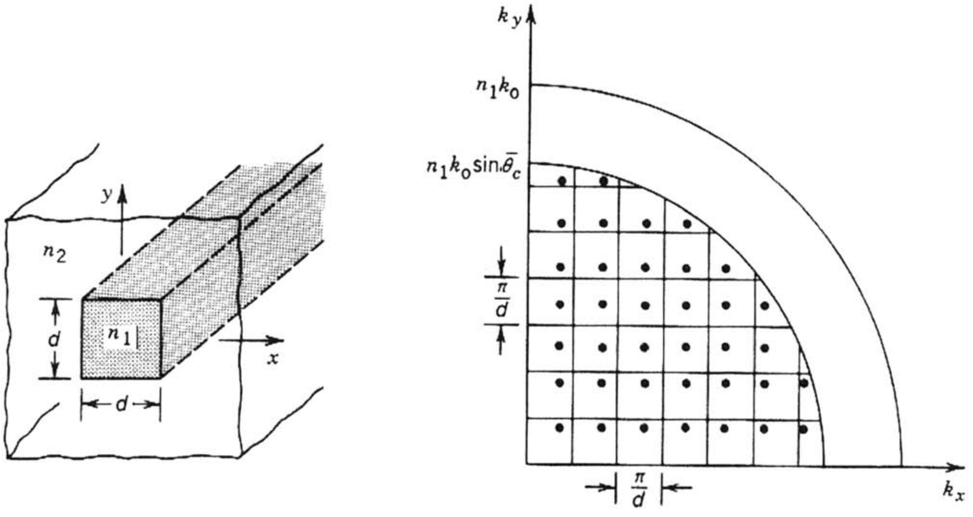

Figure 1-9: Geometry of a rectangular dielectric waveguide. The values of k_x and k_y for the waveguide modes are marked by dots. [3]

expressed

$$\begin{aligned} M &\doteq \frac{\sin\overline{\theta}_c}{\lambda/2d} \\ &= 2\frac{d}{\lambda_0}NA, \qquad (1.15) \\ \text{where } NA &= \left(n_1^2 - n_2^2\right)^{1/2} \end{aligned}$$

The symbol $\doteq$ denotes that the right-hand-side is rounded up to the nearest larger integer.

1.4.2 Two-dimensional dielectric waveguides

The number of modes in a two dimensional waveguide can be determined by simply multiplying the degrees of freedom in each axis. In Fig. 1-9, the geometry of a rectangular dielectric waveguide is shown in the left panel and waveguide modes satisfying the condition $k_x^2 + k_y^2 \leq n_1^2k_0^2\sin^2\overline{\theta}_c$ are marked with filled circles in the right panel. The number of modes are estimated to be

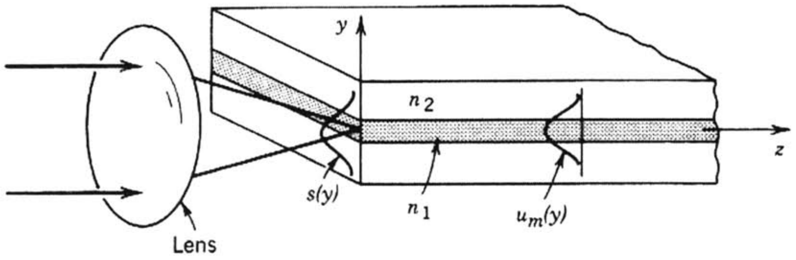

Figure 1-10: Coupling an optical beam into a waveguide. [3]

$$M \approx \frac{\pi}{4}\left(\frac{2d}{\lambda_0}\right)^2 NA^2, \tag{1.16}$$

where $NA = (n_1^2 - n_2^2)^2$, the numerical aperture.

Eqn. 1.16 can be extended for a waveguide with non-square cross section, for example, d_1 by d_2.

$$M \approx \frac{\pi}{4}\left(\frac{2d_1}{\lambda_0}\right)\left(\frac{2d_2}{\lambda_0}\right) NA^2, \tag{1.17}$$

1.4.3 Input coupling in optical waveguides

Since the dimension of optical waveguides is usually very small - down to a few micrometers, the coupling loss is usually one of major issues in focusing external light into a waveguide.

Mode excitation If the external light source has a distribution that matches exactly that of a specific mode, only that mode is excited. Generally a source of arbitrary distribution $s(y)$ excites different modes by different amounts. (Fig. 1-10) We can write $s(y)$ as superposition of different modes with their corresponding amplitudes.

$$s(y) = \sum_m a_m u_m(y), \tag{1.18}$$

where $u_m(y)$ is the transverse distribution and a_m is the amplitude. Subscript m denotes the mode number m. The coefficient a_l is given by

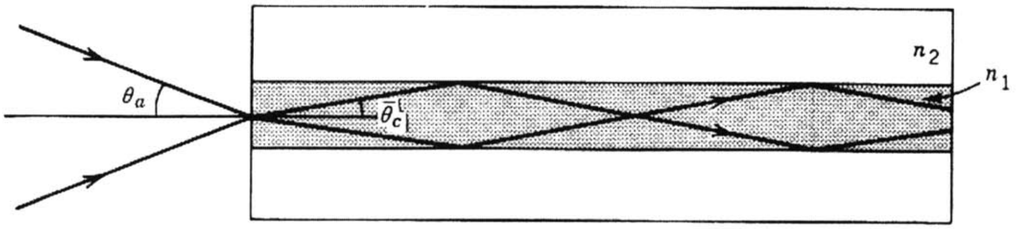

Figure 1-11: Focusing rays into a multimode waveguide. [3]

$$a_l = \int_{-\infty}^{\infty} s(y) u_l(y) dy. \tag{1.19}$$

For maximum coupling efficiency, the distribution and polarization of incident light should exactly match those of the desired mode. For example, in a single mode waveguide, if the input light does not math the single allowed mode, the intensity components corresponding to higher modes are not coupled into the waveguide, which leads to the coupling loss.

Input Couplers In order that the optical wave is guided by total internal reflection, the bounce angle should not be larger than $\overline{\theta}_c = \cos^{-1}(n_2/n_1)$. (Fig. 1-11) For maximum coupling efficiency, all of the coupled light should be guided by total internal reflection and the incident light should be focused to an angle not greater than

$$\theta_a = \sin^{-1} NA = \sin^{-1} \sqrt{n_1^2 - n_2^2}. \tag{1.20}$$

If the incident light is focused too tightly, light beams farther from the beam axis may not be coupled due to the incident angle larger than θ_a in Eqn. 1.20.

1.5 Thesis outline

In this thesis, we present major components of the integrated mode-locked lasers on Si-chips. We also introduce test setups and techniques used to examine their performance.

In Chapter 2, we review the previous work on the SiGe-SBR (Silicon Germanium Saturable Bragg Reflector). Then we show how we could improve the performance of the previous SBR by putting resonant coatings on top. We also suggest new fabrication processes which are simpler or more widely applicable than those used for the previous work.

In Chapter 3, erbium-ytterbium glass lasers with two configurations are introduced. We build these bulk lasers to verify that the fabricated SBRs are working as intended. Detailed lab techniques to successfully build the setup are also included.

In Chapter 4, we examine erbium-doped waveguide chips from Inplane Photonics Inc. to make sure that they can be used as the gain of integrated mode-locked lasers.

In Chapter 5, we make the conclusion of this thesis and explain the future work.

Chapter 2

Silicon-Germanium Saturable Bragg Reflector

A Saturable Bragg Reflector (SBR) can be used to passively mode-lock a laser by its intrinsic property of an intensity-dependent reflectivity. An SBR is composed of an absorber layer on the dielectric mirror stack. For the absorber layer, III-V compound semiconductor materials began to be used first, but nowadays research on column-IV semiconductor such as Si or Ge is actively going on for the purpose of pursuing compatibility with CMOS process. The issues which I will focus on in designing SBRs using Si and Ge are nonsaturable loss, saturable loss, two photon/free carrier absorption, and thermal conductivity.

- Nonsaturable loss

  There are two kinds of losses for a saturable absorber: saturable loss and nonsaturable loss. Saturable loss, or (maximum) modulation depth is the maximum amount of saturable absorption by the absorber and nonsaturable loss is the residual loss for an incident pulse energy density much larger than the saturation fluence [17]. A saturable absorber should have as low nonsaturable loss as possible since the nonsaturable loss is attributed to the overall loss of the cavity. Included in nonsaturable loss are the reflectivity of the bottom mirror under the absorber layer, scattering losses resulting from imperfect smoothness of the sample surface. In order to minimize nonsaturable loss, the top surface should be as smooth as possible and the reflectivity of the bottom mirror should be as high as possible.

- Saturable loss or modulation depth

  This value is recommended to be as high as possible since the pulse width is typically inversely proportional to the modulation depth. The larger the modulation depth is, the shorter the pulse.

- Two photon and free carrier absorption coefficients

  The reflectivity of a saturable absorber generally increases with higher intensity. However, when the intensity exceeds some level, the reflectivity can start to decrease by nonlinear processes like two photon absorption (TPA) or free carrier absorption (FCA). TPA is a process where two photons absorbed simultaneously, exciting an atom or ion to upper state. TPA is significant only with high optical intensities and the TPA coefficient is proportional to the optical intensity: $\alpha = \beta I$. FCA is a process where an absorbed photon impart its energy to an electron in a given band, causing it to move higher within that band. An electron in the conduction band, for example, can absorb an photno and move to a higher energy level within the conduction band. [3]

  TPA and FCA phenomena can balance the rise of pulse energy caused by noise fluctuations before the gain saturation suppresses the pulse energy rise. TPA and FCA are important nonlinear processes for saturable absorbers design because these processes can help preventing Q-switched mode-locking by lowering the pulse energy threshold for CW mode-locking specified in Eqn. 1.10.

- Thermal conductivity

  A saturable absorber actually 'absorbs' some part of the intracavity power. Therefore it is important that the saturable absorber, dielectric mirror, and substrate have as high a thermal conductivity as possible. This will prevent the buildup of temperature gradients in the structure and their accompanying

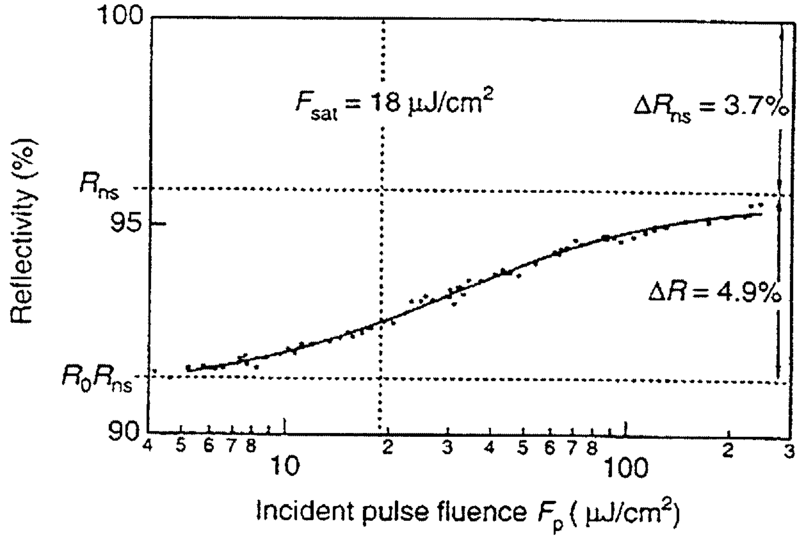

Figure 2-1: Measured nonlinear reflectivity as a function of the pulse fluence F_p. [17]

distortions. In high power applications, this is especially important to prevent thermally induced damage to the SBR.

Fig. 2-1 shows the measured nonlinearity of an SBR, denoting the modulation depth ΔR, the nonsaturable loss ΔR_{ns}, the saturation fluence F_{sat}, the high intensity reflectivity R_{ns}, and the low intensity reflectivity R_0R_{ns}.

The measured data can be fitted to

$$R_f = \frac{R_0R_{ns}}{R_0 - (R0 - 1)\exp(-F_p/F_{sat})} \tag{2.1}$$

to find the saturation fluence F_{sat}.

2.1 Previous work

In a previous work [22], Si-SiO$_2$ pairs were used for the high reflectivity dielectric mirrors. Due to the high index contrast, Si-SiO$_2$ pairs provide broad bandwidth and fewer number of pairs can be used to give the same reflectivity compared to other combinations with lower index contrasts.

One of the major challenges to fabricate Si-SiO$_2$ mirror pairs was to lower the roughness of the top surface and to minimize the scattering loss. As more layers are

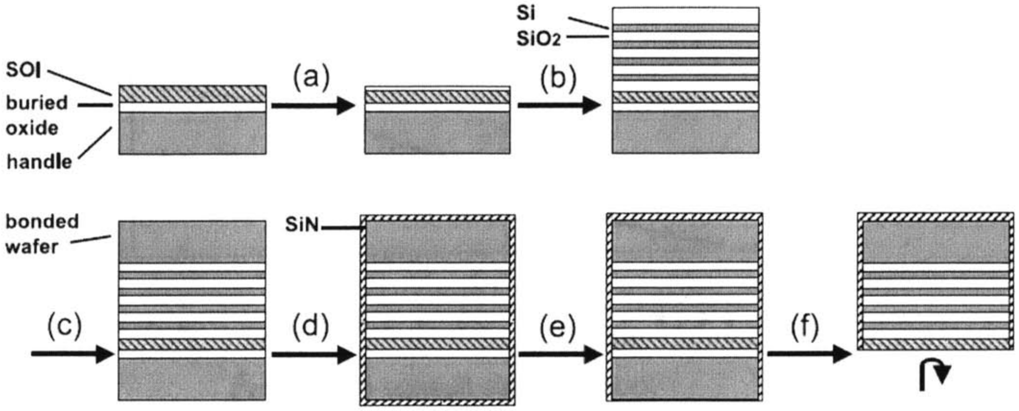

Figure 2-2: Fabrication process of the Si-SiO_2 mirror [11]

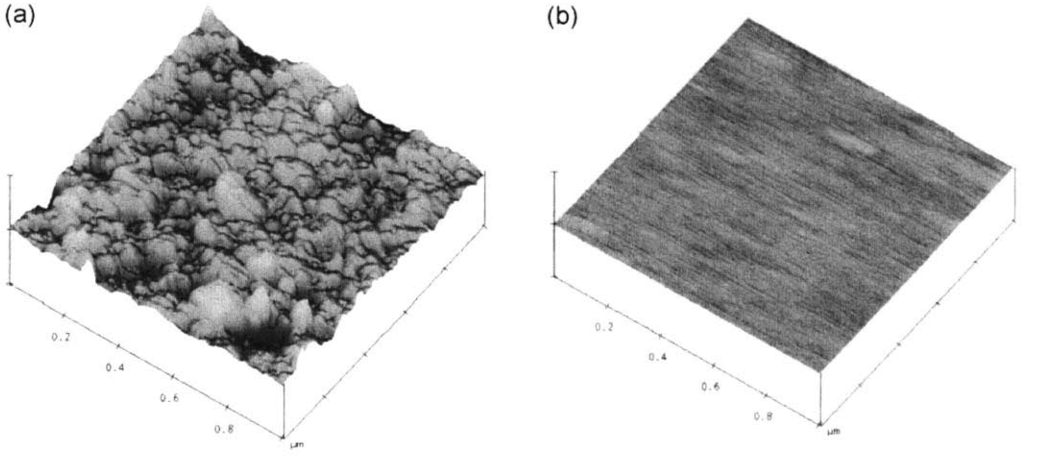

Figure 2-3: AFM images of the reflector surface. Z-axis denotes the surface level. (a) 6-pair mirror after deposition and before reversal of layer sequence. (b) Si-SiO_2 Bragg mirror deposited on a regular Si wafer after substrate removal. Courtesy of Shoji Akiyama [11]

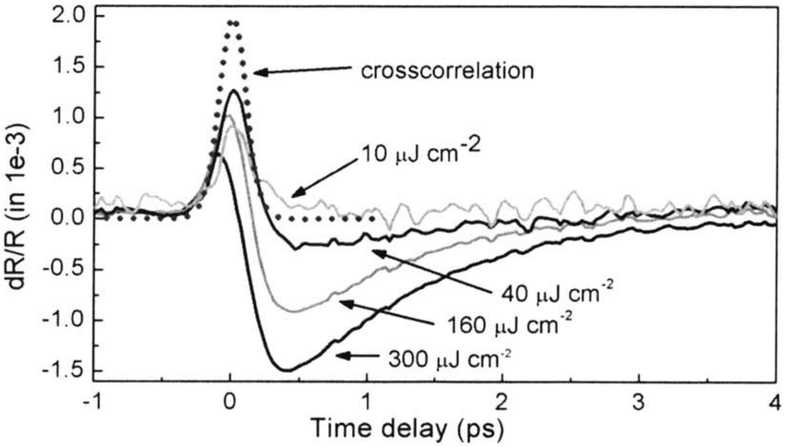

Figure 2-4: Pump-probe traces of the SiGe-SBR taken at various fluence values (solid) along with the cross-correlation of the pump probe laser source (dashed). Courtesy of Juliet Gopinath and Hanfei Shen. [11]

deposited, the surface roughness increases since small roughness of each layer is added up. This makes it impossible to keep the reflectivity high enough. In order to obtain smoother top surface, the Si-SiO_2 mirror stack was flipped vertically after another wafer was bonded on top of it and then the Si handle and silicon oxide of the original SOI (Silicon-On-Insulator) wafer was chemically etched (Fig. 2-2) [22]. As a result, the top silicon layer could be crystalline and very smooth. The surface roughness of top surface could be reduced from 10.9nm to 0.136nm in 1 μm^2 area, compared to the case of not flipping the mirror stack. Fig. 2-3 shows the improvement of surface roughness through AFM images.

Germanium which is compatible with the CMOS process was used as the saturable absorber layer material. The germanium layer was deposited on the top silicon layer and a protective SiO_2 layer was additionally deposited to make the field intensity of the standing wave at the top surface as close to zero as possible.

Fig. 2-5 shows the measured reflectivity of Si-SiO_2 Bragg mirror with and without germanium layer. For the Bragg mirror with germanium, the modulation depth was 0.3% and the nonsaturable loss was 0.17%.

The nonlinear response of the device was characterized by Juliet Gopinath and Hanfei Shen of Professor Ippen's group at MIT in a series of pump-probe measure-

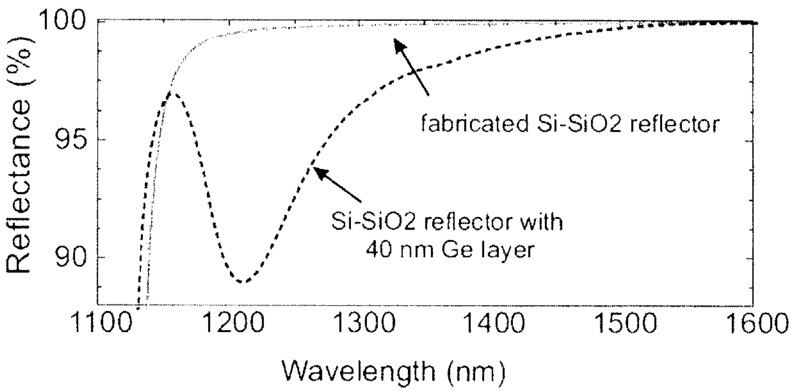

Figure 2-5: Measured reflectivity of the 6-pair Si-SiO_2 Bragg mirror with and without germanium layer. [11]

ments with 150 fs pulses centered at 1540 nm from an optical parametric oscillator (Fig. 2-4). For low to medium fluence values (e.g. 40 $\mu J/cm^2$), we observe sub-picosecond recovery of the bleaching with up to 0.13% of modulation depth. [11]

2.2 Resonant coatings

As we want to have a higher repetition rate for a mode-locked laser, the fluence on the saturable absorber decreases for two reasons.

First, the length of cavity should become smaller since the repetition rate of pulse trains is inversely proportional to the cavity length. Consequently if mirrors stay with same curvature, the spot size on the absorber gets larger. This causes smaller fluence for a given pulse energy.

Second, the higher repetition rate reduces the pulse energy when we assume that the intracavity power remains same. The fluence decreases for a given spot size on the absorber.

If the fluence is not high enough on the absorber surface, a mode-locked laser is more likely to fall into the Q-switched mode-locked regime instead of continuous wave mode-locked operation.

In order to overcome this problem, the necessary fluence for a saturable absorber to be CW mode-locked was lowered by putting additional coatings which enhances

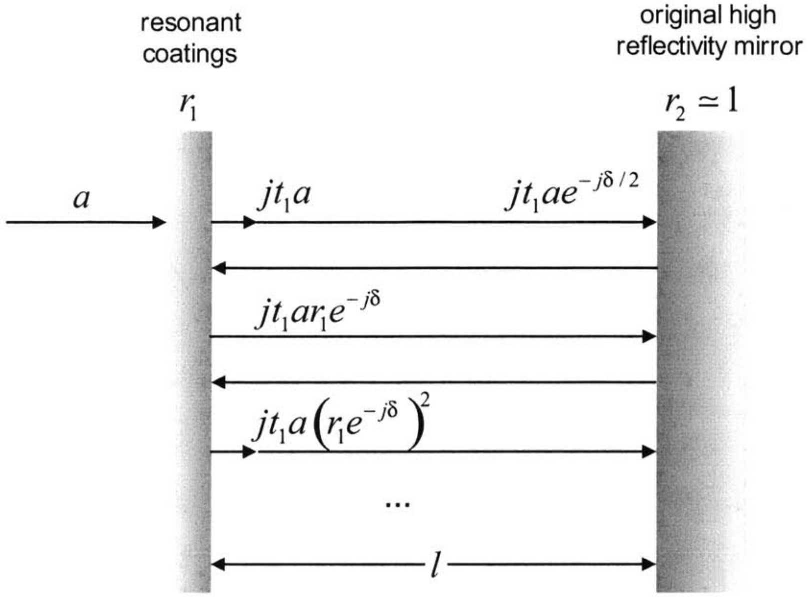

Figure 2-6: Schematic of reflections and transmission in resonantly-coated SBR structure

the field intensity around the absorber layer. These coatings are called the resonant coating. A resonantly-coated SBR has lower saturation fluence and bigger modulation depth than those of an SBR without resonant coating since the field intensity at the absorber layer is increased.

2.2.1 Physics of resonant coating

This subsection explains how resonant coatings enhance the field intensity in the absorber layer. Fig. 2-6 shows the schematic of a simple model for a resonantly-coated SBR. The left dark box denotes the resonant coatings and the right dark box the high reflectivity mirror. In the space between those two dark boxes is the absorber layer. The model forms a sort of Febry-Perot resonator. If we assume the reflectivity of the resonant coatings is r_1 and the reflectivity of the bottom mirror is close to 100%, the field amplitude inside is given by

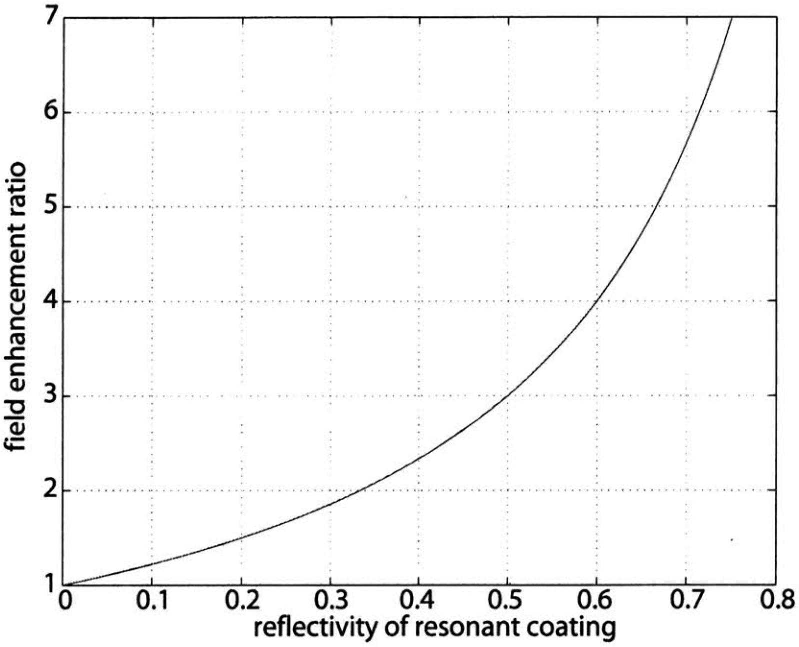

Figure 2-7: The ratio of field intensity of SBR with resonant coatings to that of SBR without resonant coatings at the absorber layer

$$\begin{aligned} a_{eh} &= jt_1 a + jt_1 a r_1 e^{-j\delta} + jt_1 a \left(r_1 e^{-j\delta}\right)^2 + \cdots \\ &= \frac{jt_1 a}{1 - r_1 e^{-j\delta}}, \end{aligned} \tag{2.2}$$

where a denotes the incoming filed amplitude, t_1 the transmissivity of the resonant coatings, and δ the phase change over one round trip. The enhancement of field intensity is

$$R_{eh} = \frac{|a_{eh}|^2}{|a|^2} = \frac{t_1^2}{1 + r_1^2 - 2(\cos\delta) r_1}.$$

In order to maximize R_{eh}, the thickness l of absorber layer is set to give $\delta = 2m\pi\,(m = 1, 2, \cdots)$. The maximized R_{eh} is

$$\boxed{R_{eh} = \frac{1 - r_1^2}{(1 - r_1)^2},} \tag{2.3}$$

and is plotted in Fig. 2-7.

Table 2.1: Absorption and peak field intensity depending on the number of layers of resonant coatings. The intensity of incident beam is set to 100% for a relative comparison.

	No coating	3-layers	5-layers
Absorption at 1550nm	0.75%	1.6%	3.0%
Peak field intensity in Ge layer	32%	67%	130%

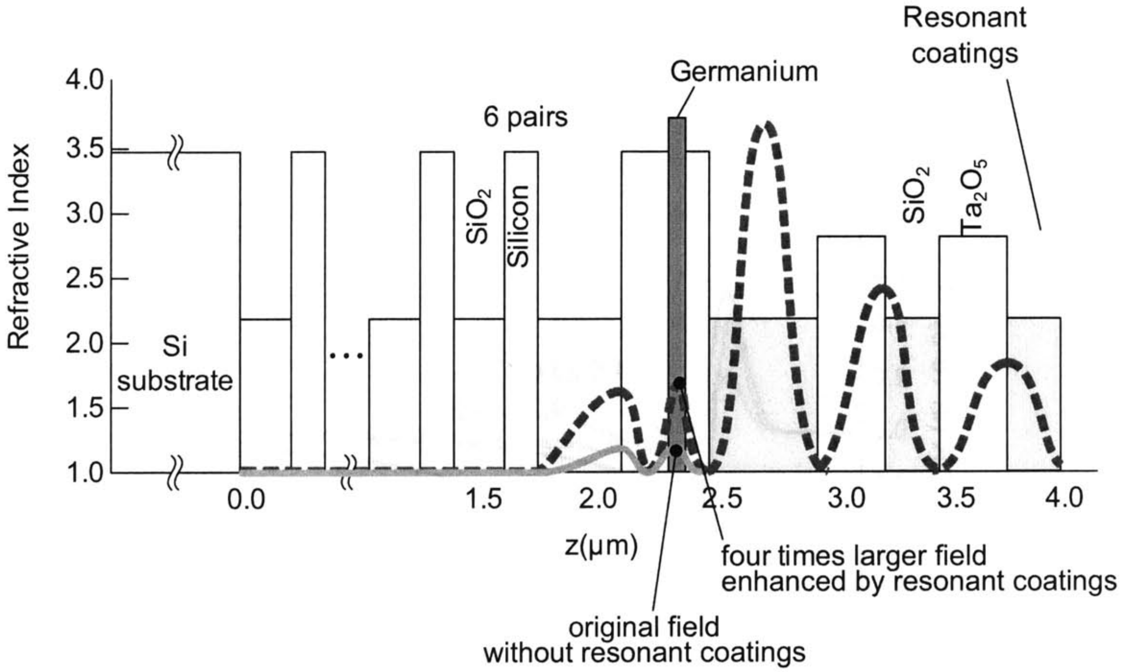

Figure 2-8: Structure of SiGe-SBR with five layers of resonant coatings

2.2.2 Design and fabrication of resonant coatings

Two kinds of resonant coatings were designed, three-layer structure and five-layer one. As more layers are deposited for resonance, the reflectivity of the coatings increase and the field in the absorber layer is more enhanced as shown in the previous subsection. Target field intensity for those resonant coatings is shown in Table 2.1. The figures in Table 2.1 are simulation results from the OptiLayer software. We can see that the peak field in the germanium layer almost doubles when one pair of resonant coatings is added.

In order to achieve the field enhancement in Table 2.1, resonant coatings were

Table 2.2: Layer thickness for resonant coatings.

	3-layers	5-layers
Original SBR	-	-
SiO_2	534nm	560nm
Ta_2O_5	181nm	190nm
SiO_2	267nm	280nm
Ta_2O_5	0nm	190nm
SiO_2	0nm	280nm
Air	-	-

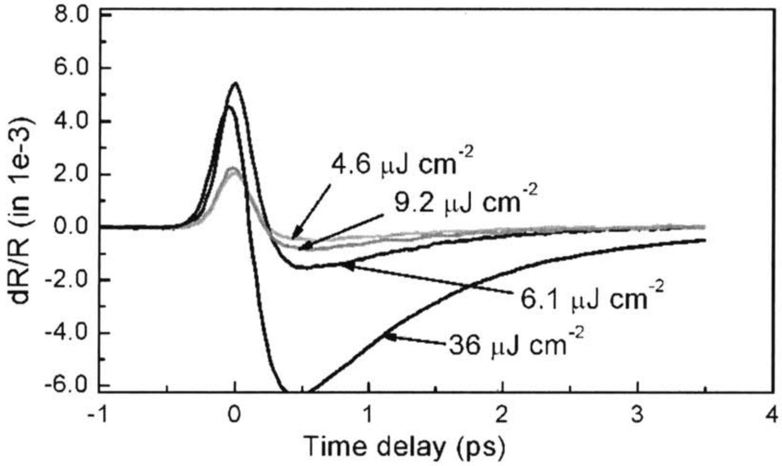

Figure 2-9: Pump-probe traces of the resonantly-coated SiGe-SBR taken at various fluence values

deposited on the original SBR structure by Peter O'Brien at MIT Lincoln Laboratory (Fig. 2-8). The thickness of each coating is specified in Table 2.2. The low-index material closer to the original structure starts with half wavelength thickness and the subsequent layers are quarter wavelength thick to function as a reflector.

2.2.3 Measurement

The reflectivity could not successfully be measured. When the resonant coatings were deposited on the original SBRs, the samples were only 3mm×3mm, too small to be mounted for a spectro photometer which can give accurate absolute reflectivity close to 100%. A sample should be larger than 1cm in diameter to produce reliable data in the spectro photometer since the beam in the machine is of that size. Thus an FTIR (Fourier Transform Infrared) spectrometer was used instead with which a smaller sample can be mounted for measuring the reflectivity. However, FTIR failed to provide trustable absolute reflectivity. The measured reflectivity showed deviation as large as 10% depending on samples. Preparing larger piece of sample and using a spectro photometer would help measuring the reflectivity more accurately.

The nonlinear response of the device was characterized by Felix Grawert and Ali Motamedi using a pump-probe measurement setup with 150fs pulse centered at 1540nm (Fig. 2-9). A fluence of 9.2 $\mu J/cm^2$ was needed to give maximum modulation depth of 0.52%. This modulation depth is four times larger than that of the previous SBR and the corresponding fluence is four times smaller. [7] This measurement results agree with the simulation where the field intensity was enhanced by factor of four.

The fabricated SBR with resonant coatings was tested in a cavity for 340MHz erbium-ytterbium glass laser (Fig. 3-16).

Although resonant coatings can provide enhanced absorption and modulation depth, they can bring unwanted side effects. With those resonant coatings, the field intensity increases not only in the absorber layer but also in the neighboring layers. The increased intensity in the neighboring layers can cause larger nonsaturable loss which can destabilize CW mode locking. Therefore it is important to use material with as low loss as possible.

2.3 New fabrication procedures

The fabrication process described in Fig. 2-2 showed satisfactory performance in terms of surface roughness, reflectivity, and saturable absorption. However, the process which included wafer bonding and polishing left much room for improvement for simpler fabrication steps. This section introduces new fabrication schemes and examines their advantages and disadvantages.

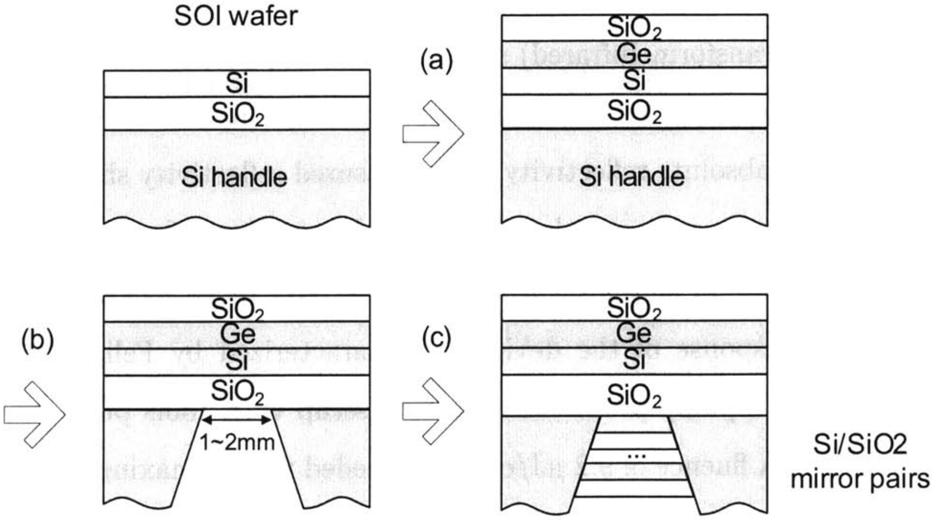

Figure 2-10: Fabrication process of SBR without using a second wafer

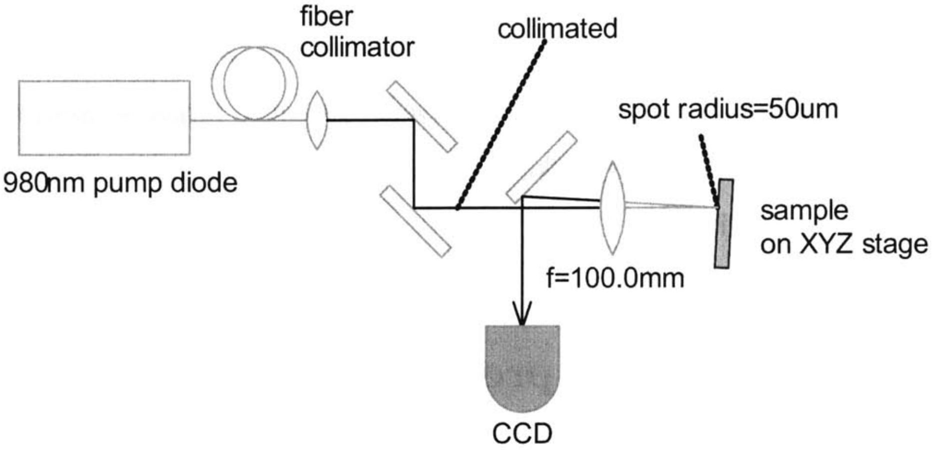

Figure 2-11: Schematic of experimental setup to examine reflected images from an SBR sample

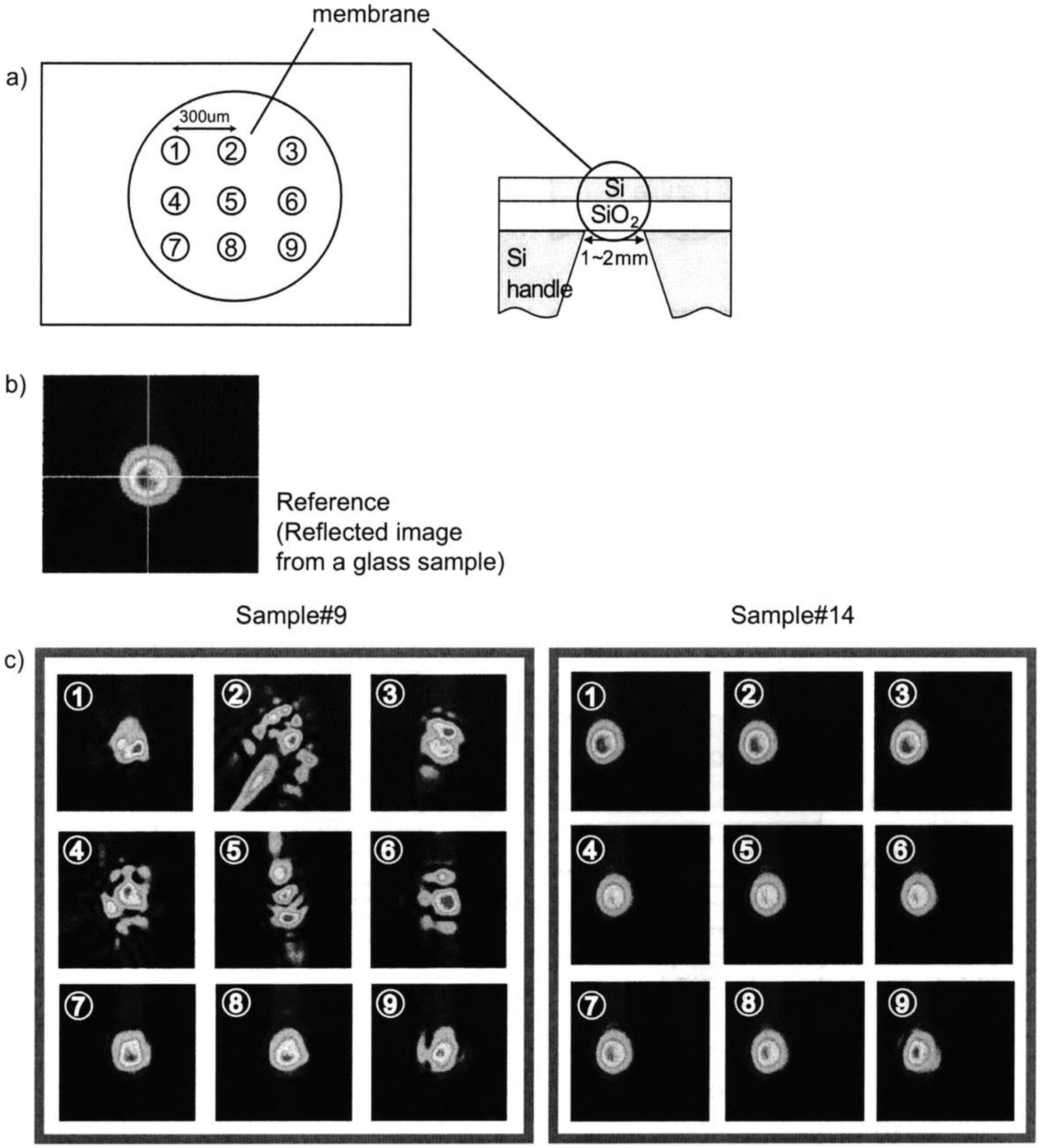

Figure 2-12: Reflected beam images from Si/SiO_2 membrane samples. a) Top view and cross-sectional view of a sample. Measured spots are numbered from 1 to 9. b) Reflected beam image from a flat glass. c) Reflected beam images for nine different spots on each of two samples.

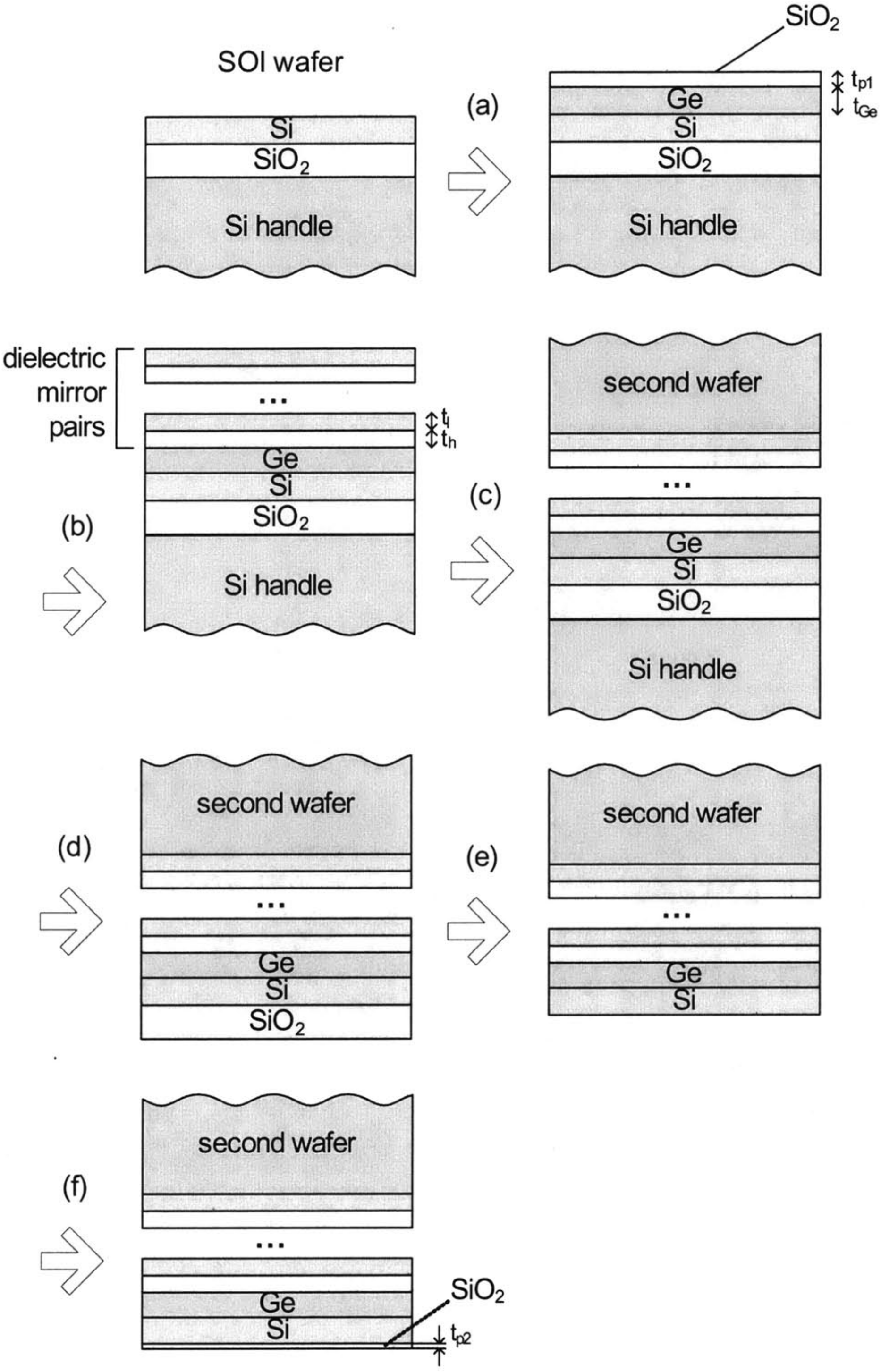

Figure 2-13: Suggested fabrication process of SBR with in which Ge layer is deposited earlier than other processes and another wafer is bonded.

2.3.1 Fabrication

The first try to simplify previous fabrication process is shown in Fig. 2-10. In step (a), a germanium layer is grown on top of crystalline silicon of an SOI (Silicon On Insulator) wafer and then a protective SiO_2 layer is deposited. Step (b) includes etching a back-hole of 1~2mm diameter on the bottom of the SOI wafer. In step (c), high reflectivity mirror pairs are deposited on the bottom. After these steps, the whole structure becomes an SBR and a second wafer is not necessary. This process may be much simpler than the previous one.

For a preliminary test to figure out whether such fabricated structure can function as a saturable absorber, reflected beam images from the samples were examined. In order that the surface of the fabricated absorber is smooth enough, at least the reflected beam images should look the same as the incident beam images. In the experimental setup of Fig. 2-11, a collimated 980nm beam is focused on the sample to be examined with spot size of 50μm. The reflected beam is directed into a CCD camera to inspect its profile.

Fig. 2-12 shows the structure of examined samples, reference beam shape which was reflected from a flat glass, and captured reflected beam images from 18 spots of two samples. The examined samples here have Si-SiO_2 membrane over a circle of 1~2mm diameter with thickness of about 0.5μm. As shown in Fig. 2-12 c), the reflected beam image had very different profile for each spot on each sample. This means that the surface of the membrane was rough or wrinkled by the strain of the layers in the membrane. This phenomena did not disappear even after germanium and its protection layer were deposited to expect a more stable membrane. Thus the fabrication process in Fig. 2-10 turned out not to be adequate for a saturable absorber.

Due to the instability of the membrane structure, we had to resort to bonding a second wafer before removing the original Si wafer. This change sounds much like the previous fabrication plan in Fig. 2-2. However, this new fabrication plan solves another problem of the previous plan. For some reactor machines, germanium cannot be grown after dirty processes such as wafer bonding. Actually Professor Judy Hoyt's lab does not allow a sample that has been in a dirty process to be put inside the reactor.

Thus a new fabrication plan was suggested (Fig. 2-13). With an SOI wafer given, germanium and its protective layer (SiO_2) are deposited on the crystalline silicon layer in step (a). The protective layer is not necessary for SBR operation, but it prevents further deposition from inter-diffusing with the germanium layer. The inter-diffuse can decrease the absorption of the germanium. In step (b), dielectric material pairs with alternating higher and lower refractive indices are deposited to function as a high reflectivity mirror. In step (c), a second wafer is bonded on top of the dielectric mirror and in step (d), the original wafer is removed. Through the steps (c) to (f), the original SiO_2 layer in the SOI wafer is etched and new thinner SiO_2 layer is deposited for protection purpose.

2.3.2 Material selection for the high reflectivity mirror

One of the major issues in selecting materials for the high reflectivity mirror is thermal conductivity. It is important for an SBR structure to transfer the absorbed power to the bottom with proper conductivity, so that the whole structure is not distorted by the remaining heat. When we consider the heat transfer of the entire SBR structure, we assume that the thermal conductivity of the crystalline silicon and the substrate is high enough. Thus the thermal conductivity of dielectric mirror is dominant. With the given definition of the thermal conductivity

$$k = H \times \frac{L}{A\Delta T}, \tag{2.4}$$

where H is heat flow rate, L is distance, A is area, ΔT is temperature difference. The total temperature difference over the mirror structure with n pairs of high refractive index material and low one is given by

$$\Delta T_{total} = \sum_{i=1}^{2n} H \times \frac{L_i}{Ak_i} = \frac{H}{A} n \left(\frac{L_h}{k_h} + \frac{L_l}{k_l} \right), \tag{2.5}$$

Table 2.3: The properties of dielectric materials.

	a-Si	TiO_2	SiO_2
L (physical thickness for $\lambda/4$) [nm]	107	177	260
k (thermal conductivity[a]) [W/mK]	149	6.7	1.3

---

[a] These thermal conductivities are for bulk material. For thin films, these values may be reduced.

Table 2.4: Comparison between two types of SBR: SBR using a-Si/SiO_2 pairs versus SBR using TiO_2/SiO_2 pairs for high reflectivity mirrors.

		a-Si/SiO_2 SBR	TiO_2/SiO_2 SBR
Refractive index		3.6/1.45	2.22/1.45
Number of pairs		5	9
ΔT_{total} [a]		$46K$	$91K$
ΔR_{ns} [b] (Nonsaturable loss)	no resonant	0.98%	0.25%
	3 layers	2.13%	0.57%
	5 layers	4.22%	1.06%
ΔR [c] (Absorption by Ge)	no resonant	0.41%	0.45%
	3 layers	0.90%	0.91%
	5 layers	1.72%	1.80%

---

[a] Assumed H=100mW (2% absorption from 5W intracavity power) and $A = \pi(30\mu\text{m})^2$

[b] Simulated using OptiLayer.

[c] Simulated using OptiLayer.

where L_h is the thickness of the high index material, L_l is the thickness of the low index material, k_h is the thermal conductivity of the high index material, and k_l is the thermal conductivity of the low index material.

Table 2.3 shows the material properties of amorphous silicon (a-Si), TiO_2 and SiO_2. Based on these properties, a-Si/SiO_2 pairs and TiO_2/SiO_2 pairs are compared to each other in terms of thermal conductivity and loss in Table 2.4.

a-Si/SiO_2 pairs have larger index contrast between two materials than TiO_2/SiO_2 pairs do. This is why a-Si/SiO_2 pairs need less number of pairs to produce the same amount of reflectivity and consequently give broader bandwidth. The temperature

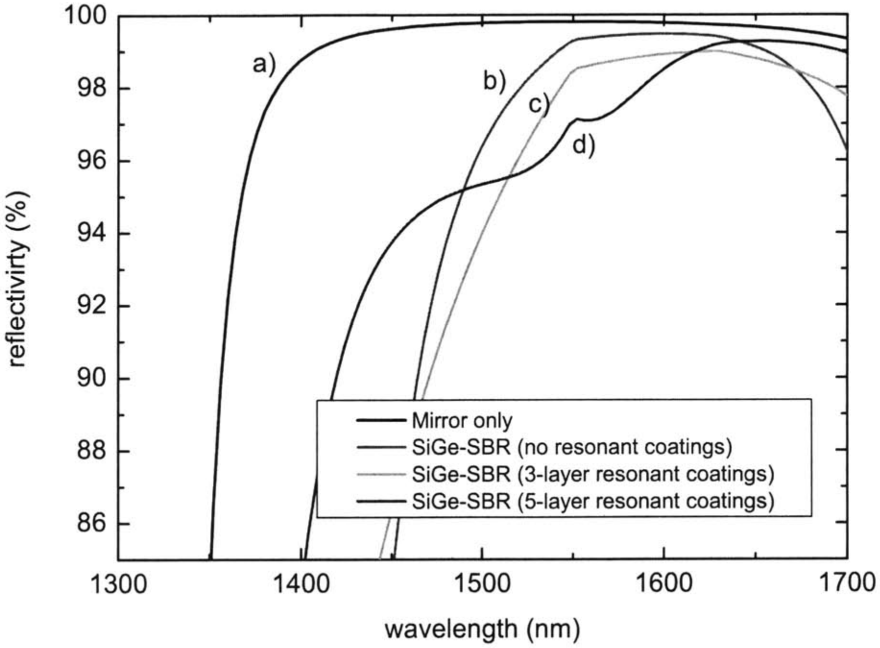

Figure 2-14: Reflectivity for the designed SiGe-SBR. a) Mirror-only structure. (9-pairs of TiO_2/SiO_2 layers) b) SiGe-SBR c) SiGe-SBR with 3-layers of resonant coatings d) SiGe-SBR with 5-layers of resonant coatings

difference over the mirror structure ΔT_{total} was evaluated using Eqn. 2.5 and the data in Table 2.3. The temperature difference for TiO_2/SiO_2 pairs was about two times higher since TiO_2 is poorer thermal conductor than a-Si and TiO_2/SiO_2 pairs are thicker. From the Table 2.4, we can note that a-Si/SiO_2 pairs transfer heat twice better than TiO_2/SiO_2 pairs do.

On the other hand, a-Si/SiO_2 pairs showed four times larger nonsaturable loss when the absorption by germanium was the same. With five layers of resonant coatings on the SBR based on a-Si/SiO_2 mirror, the nonsaturable loss was larger than 4% which is not negligible.

In summary, if the temperature difference of $91K$ is tolerable on the SBR, TiO_2/SiO_2 pairs work better in terms of the nonsaturable loss, still giving enough bandwidth (although not shown in this thesis).

2.3.3 Expected reflectivity

Fig. 2-14 shows the simulated reflectivity of SBRs which would be fabricated using the process described in Fig. 2-13.

Chapter 3

Erbium-ytterbium:glass bulk laser

Erbium-ytterbium (ErYb) glass bulk lasers were built to assess the functionality of the saturable absorbers that were designed in chapter 2. The lasers are passively mode-locked using the designed absorbers. This chapter shows how various parameters were determined to set up the bulk lasers and the laser output is characterized.

In those lasers, the gain medium was a glass co-doped with erbium and ytterbium. While building the cavity, the main issue was to build it with gain spectrum as flat or broad as possible over the C-band (1535$\sim$1560nm) so that the broad bandwidth of the saturable absorber can be fully utilized.

In order to obtain the flattest gain spectrum, we can engineer the doping level of ErYb glass, the spot size of pump beam, cavity loss or output coupling ratio, the length of gain medium. In [14] it was shown that the gain spectrum is highly dependent on the normalized population of the upper laser level β (Fig. 3-1). The larger β is, the more populated the upper laser level becomes. Details of the cavity adjustment to optimize the gain spectrum is shown in the following two sections.

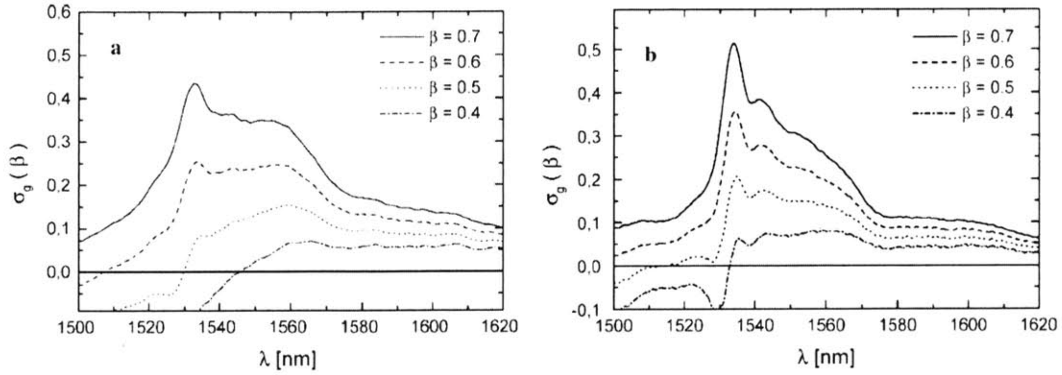

Figure 3-1: Effective gain cross sections for (a) fluoride phosphate and (b) phosphate glass for different inversion levels [14]

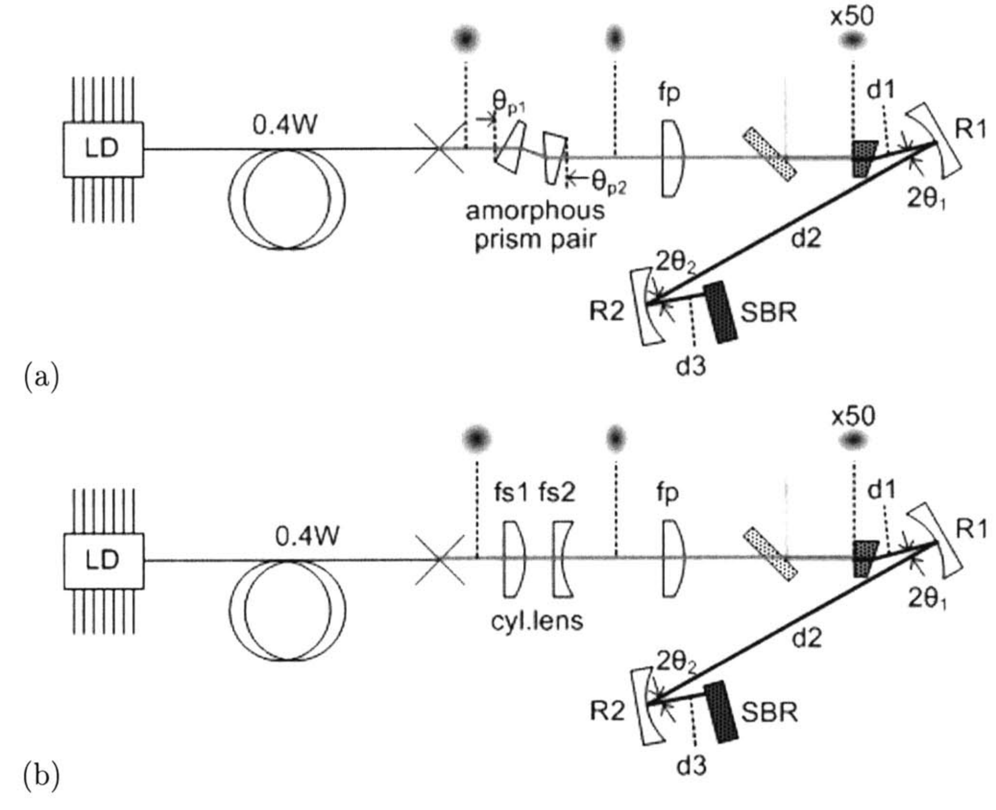

Figure 3-2: The schematic of ErYb glass laser with V-cavity configuration. (a) Amorphous prism pair was used to shape the pump beam. (b) A pair of cylindrical lens were used to shape the pump beam.

3.1 V-cavity

3.1.1 Design

The first cavity was a V-cavity design where the gain medium is located at one end of the cavity, as shown in Fig. 3-2(a),(b). The cavity is composed of pump optics to excite the gain medium with a proper beam profile and cavity itself to trap the stimulated emission. The difference between two setups in Fig. 3-2(a) and (b) is how the pump beam was shaped.

Pump Optics

In Fig. 3-2(a), 0.4W 980nm pump beam from InGaAs laser diode is connected to single mode fiber and then a collimator. The collimated pump beam goes through a pair of amorphous prism to be shaped into ellipsoid with circularity of 0.67 (longer vertical radius). The prism pair shrinks the beam along the tangential plane.[1] The circularity was determined such that laser beam is as circular as possible in the cavity outside of the gain medium. (section 3.1.1)

Two prisms are aligned such that the incident angles toward the flat cut prism surfaces are θ_{p1} and θ_{p2}, respectively. θ_{p1} and θ_{p2} can be determined to obtain desired circularity. One thing to be careful is that there are many combinations of θ_{p1} and θ_{p2} that give us the desired circularity, but even if the circularity after the prism pair is same for various prism angles, the distance between tangential focal point and sagittal focal point can be different after the beam is focused. For this reason, the prism angles should be carefully chosen to minimize the separation between tangential and sagittal focal plane after lens fp. The elliptically shaped beam is focused by a plano-convex lens with effective focal length fp=75mm.

The major problem of shaping the pump beam using a pair of prisms was the separation between tangential and sagittal focal plane. After the beam is focused by lens fp, the focal points of tangential and sagittal plane can not be closer to each

---

[1] Tangential plane indicates the plane parallel to the floor. The plane perpendicular to both the floor and the beam is called sagittal plane.

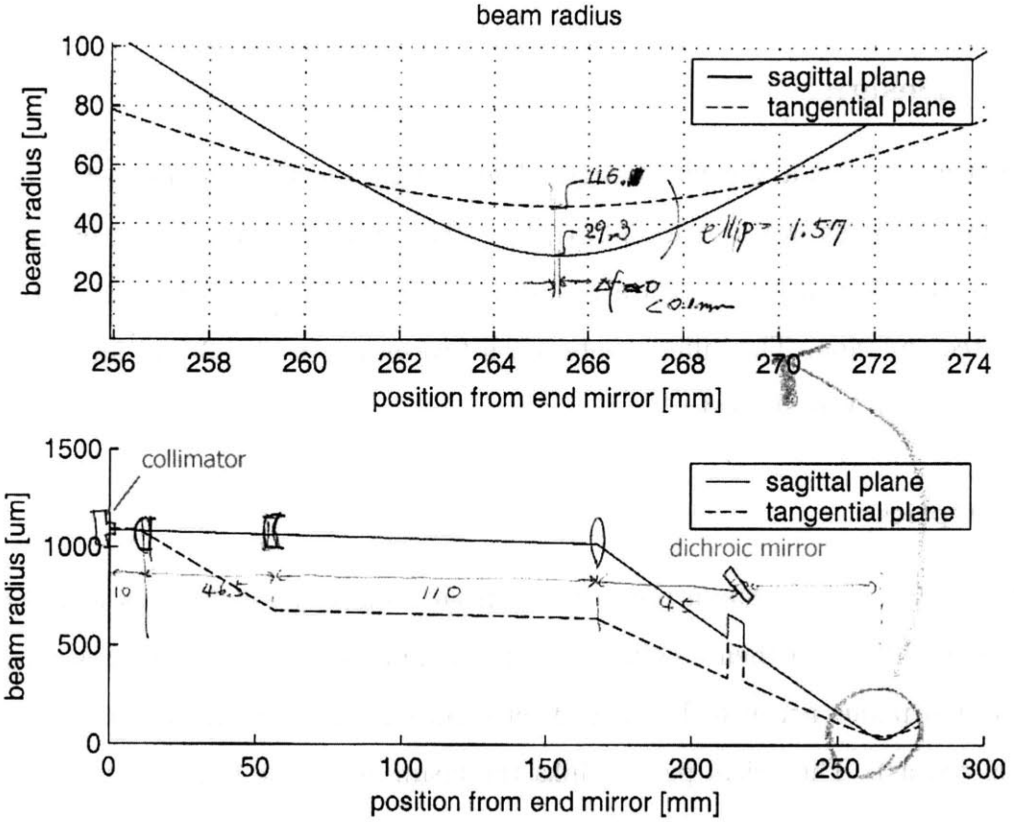

Figure 3-3: Beam profile along the pump optics.

other than 1.5mm. This prevented the focused spot from having the desired beam profile and pulled down the maximum output power and/or bandwidth of the laser beam.

In order to solve the focal point separation problem, two cylindrical lenses were utilized instead of the prism pair. The cavity with pump optics using cylindrical lenses is shown in Fig. 3-2(b). The focal length of each cylindrical lens was fs1=130mm (plano-convex) and fs2=-80mm (plano-concave), and the distance between the two lenses was 47.1mm. In this way, the spot size at the left end of the gain could be 22x37μm and the distance between tangential focal point and sagittal focal point was less than 0.1mm. In the new pump optics, fp was 75mm, too. Simulated beam profile using the cylindrical lenses is shown in Fig. 3-3.

The pump spot size at the gain medium was determined by simulating the ErYb glass laser by a laser model [20]. For the pump power of 450mW from commercial

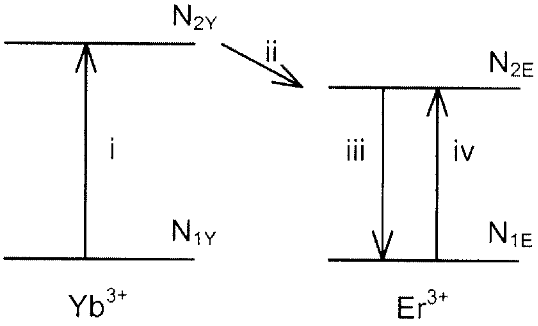

Figure 3-4: Simplified energy-level diagram of the erbium-ytterbium system

laser diodes, a pump spot size is focused to be 25μm.

A dichroic mirror is inserted after the focusing lens fp and before the ErYb glass in order to transmit the pump beam and to redirect output laser beam to the other way for other applications.

Gain medium

Characteristic ErYb glasses act as a three-level system: more than half of the erbium ions are required to be raised to the upper laser level for amplification or laser operation [14]. Ytterbium ion facilitates the absorption of pump beam and reduces pump threshold and necessary length of gain medium as well. The ErYb glass used in the experiment of this chapter was a phosphate glass (Kigre, Inc. type QX-Er) co-doped with $2.3 \times 10^{20}\mathrm{Er} - \mathrm{ions/cm}^3$ and $2.1 \times 10^{21}\mathrm{Yb} - \mathrm{ions/cm}^3$. Fig. 3-4 shows a simplified diagram of energy state and transitions in ErYb-doped glass material. N_{1Y}, N_{2Y} indicates the Yb^{3+} population of the ground state and the excited metastable level, respectively. N_{1E}, N_{2E} denotes the Er^{3+} population of the lower laser level and the upper laser level, respectively.

Eqn. (3.1), (3.2), and (3.3) describes the rate equation for erbium and ytterbium population and the photon number q [20]. The absorption (i) is caused by optical pumping and described by the first term $\sigma_Y N_{1Y} F$ of Eqn. (3.1). Erbium pumping then arises from energy transfer (ii) which is explained by the second term $kN_{2Y}N_E$ of Eqn. (3.1). Stimulated emission (iii) and re-absorption (iv) happen between the

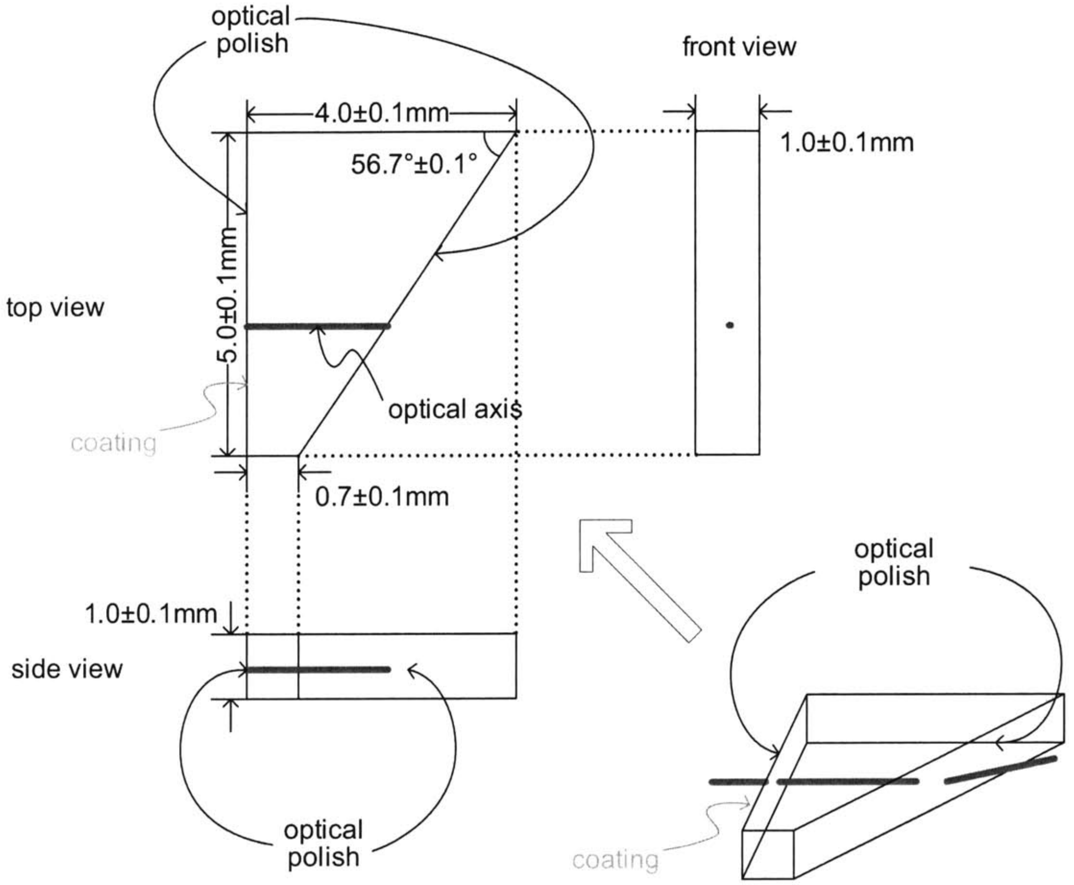

Figure 3-5: The schematic of erbium-ytterbium:glass. The left side of the glass when viewed from the top is coated for anti-reflection at 980nm and for high reflectivity at 1550nm.

upper laser level and the lower laser level. The second term $(\sigma_E c\rho/h\nu)(N_{2E} - N_{1E})$ of Eqn. (3.2) describes the stimulated emission process and the third term N_{2E}/τ_E reflects the nonradiative decay of the upper laser level population.

$$\begin{aligned} \sigma_Y N_{1Y} F - k N_{2Y} N_E &= 0 \qquad (3.1) \\ k N_{2Y} N_E - (\sigma_E c\rho/h\nu)(N_{2E} - N_{1E}) - N_{2E}/\tau_E &= 0 \qquad (3.2) \\ \sigma_E c \int_{V_a} (\rho/h\nu)(N_{2E} - N_{1E}) \mathrm{d}\mathbf{r} &= q/\tau_c \qquad (3.3) \end{aligned}$$

In Eqn. (3.1), F is the pump photon flux, σ_Y is the absorption cross section for ytterbium, and k is the rate coefficient of the energy transfer. N_E is the total erbium

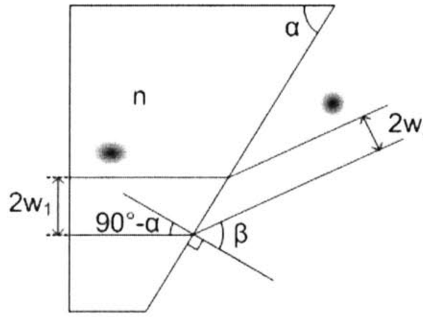

Figure 3-6: Beam shape change before and after the glass.

population, or approximately $N_{1E}+N_{2E}$. In Eqn. (3.2), σ_E is the stimulated emission cross section of the laser transition, ρ is the space-dependent energy density, τ_E is the decay time of the upper laser level, and c is the speed of light. In Eqn. (3.3), the left side denotes the rate of photon generation over the volume V_a of the active material, and the right side shows the rate of photon decay and τ_c is the photon cavity lifetime.

Eqn. (3.1), (3.2) are based on the following assumptions: up-conversion and multiphonon relaxation process are neglected. In addition, the change in ground state population of ytterbium is negligible, thus we can equate N_{1Y} with N_Y. This assumption implies a pump intensity less than 10^5W/cm^2, which is always satified in the case of cw pumping by laser diodes.

Dimension The physical length of ErYb glass along the optical axis was designed to be a few millimeters to provide enough gain. Fig. 3-5 shows the schematic of ErYb glass used in this experiment. The physical length of the gain medium along the optical axis ranges from 0.7mm to 4.0mm, depending on what part of the glass the incoming beam hits. The angle of top-right side of the glass is Brewster's angle for glass-air interface. The incoming beam gets out of the glass at Brewster's angle and the loss at the glass-air interface is minimized. The left side of the glass when viewed from the top is coated for anti-reflection at 980nm and for high reflectivity at 1550nm. The coated side also functions as an output coupler of the cavity. Two sides of the glass that contains the optical axis are polished so that the scattering loss at the surface is minimized.

Table 3.1: Parameters for the V-cavity configuration and values used in this experiment

parameter	description and constraint	typical value in this experiment
R1	The radius of curved mirror closer to the gain medium.	50mm
R2	The radius of curved mirror closer to the saturable absorber.	50mm
d1	The distance between mirror R1 and glass	$\sim$ R1/2
d2	The distance between mirror R1 and R2	$300 - 700$mm
d3	The distance between mirror R2 and SBR	$\sim$ R2/2
θ_1	The incident angle in tangential plane at the mirror R1. Determined such that the astigmatism of the gain medium is compensated.	$5 - 10°$
θ_2	The incident angle in tangential plane at the mirror R2. As small as possible. Generally mechanically limited.	$2 - 5°$

In a cavity, circular beam shape is preferred to get rid of axial asymmetry. In order that the beam in the cavity is as circular as possible, the beam shape inside the glass should be elliptical in horizontal way. Fig. 3-6 is shown to explain the beam dimension inside and outside of the glass. By Snell's law,

$$n \cos \alpha = \sin \beta, \tag{3.4}$$

where n is refractive index of the glass. Assuming that we have Brewster's angle cut (α) at the right side of the glass,

$$\sin \alpha = n \cos \alpha. \tag{3.5}$$

Using Eqn. 3.4 and Eqn. 3.5, we get $\sin \alpha = \sin \beta$ or $\alpha = \beta$. Therefore,

$$w_1 = w_2 \frac{\sin \alpha}{\cos \beta} = n w_2 \tag{3.6}$$

Cavity

In Fig. 3-2, the cavity itself is composed of the ErYb glass, two curved mirrors with radius of curvature R1 and R2, and the saturable absorber. Parameters that determine the dimension of the cavity in Fig. 3-2 are shown in Table 3.1.1. We followed the following procedures to decide the values of the parameters.

1. Set the desired repetition rate of the pulse train. The repetition rate can be limited by the necessary fluence for the saturable absorbers to make the laser mode-locked in continuous wave mode. As the repetition rate goes up, the fluence decreases because the pulse energy gets smaller and spot size on the absorber gets bigger as long as the mirror curvature remains same. Given that the repetition rate is f_R, the optical length of cavity L is

   $$L = \frac{c}{2 f_R} \tag{3.7}$$

   where c is the speed of light in free space.

   Assuming that the gain medium is very short compared to the entire cavity length, the distance between two curved mirrors is estimated to be

   $$d2 \simeq L - (d1 + d3) \simeq L - \frac{R1 + R2}{2} \tag{3.8}$$

where d2 was assumed to be large enough compared to d1 or d3.

2. Calculate necessary spot size in the gain medium and at the absorber surface. Those spot sizes need to be small enough to achieve desired performance, especially the bandwidth of mode-locked pulse.

   For gain medium - ErYb:glass in this experiment, the spot radius that gives maximum output power was around 20μm. This value is the result of numerical analysis of a ErYb microchip laser based on the model studied in [20]. In the analysis in [4], the optimum spot size was around 25μm, where the doping concentration of Erbium ion and Ytterbium ion was $1.5 \times 10^{19}\text{cm}^{-3}$ and $1.5 \times 10^{21}\text{cm}^{-3}$, respectively, and the physical length of gain medium was 2mm. Since the doping levels are different from those of the glass used in this experiment, the simulation was conducted again with the real doping levels - $2.3 \times 10^{20}\text{cm}^{-3}$ and $1.5 \times 10^{21}\text{cm}^{-3}$ for Erbium and Ytterbium, respectively, which gave us a smaller but similar optimum spot size.

   For the absorber - the upper limit of the spot size at the absorber surface is determined by necessary fluence with which the cavity is stably CW mode-locked. Given the necessary fluence F_{min} of the absorber (for example, 10 times of the saturation fluence)

$$\begin{aligned} F_{min} &= \frac{E_p}{A_{abs}} = \frac{\overline{P_{intra}}}{\pi w_a^2 f_R} \\ \therefore w_a &= \sqrt{\frac{2L\overline{P_{intra}}}{\pi c F_{min}}} \end{aligned} \tag{3.9}$$

   where E_p is the energy of each pulse, A_{abs} is the area of spot on the absorber, $\overline{P_{intra}}$ is the average intracavity power, and w_a is the spot radius on the absorber.

3. Decide R1 and R2, the curvature radii of the curved mirrors. We usually have limited choices on R1 and R2 because there are only discrete radii of the curved mirrors. In our lab, R1 or R2 should be one of 25mm, 50mm, 100mm, 200mm, and so on for immediate availability.

R1(mm)	θ_1 (deg)
25	10.9
50	7.6
75	6.2
100	5.4

Table 3.2: The astigmatism compensation angle θ_1 for various mirror curvatures. The thickness of the gain medium is 2.0mm and the refractive index of it is 1.52.

The curvature of the mirrors is decided based on the cavity length and desired spot size on the gain medium and on the absorber surface. For fixed cavity length, a mirror with stronger curvature can give us smaller spot sizes and for fixed curvature of mirror, longer cavity leads to smaller spot size.

In order to examine if some R1 and R2 can provide desired spot sizes for given cavity length, it is a good way to build a stability diagram with variations on d1 and d3. If for some R1 and R2, the range of d1 and d3 which leads to desired spot sizes can be quite strict - for example, range of less than 100μm, - although the entire range for stability is large enough. In that case, it will be very hard to align the mirrors to give desired spot sizes and more likely to have larger spot sizes than intended. To allow smaller spot sizes over larger range of d1 and d3, smaller R1 and R2 need to be adopted.

4. For the last step, decide θ_1 and θ_2.

   θ_1 exists to compensate astigmatism introduced by the gain medium and the astigmatism is compensated by putting the mirror R1 at some angle from the beam coming out of the gain medium. θ_1 is dependent on both the thickness of gain medium and the mirror curvature R1.

   The formula to decide the angle of the curved mirror is given by

$$\sin^2\theta_1 = \frac{t\sqrt{n^2+1}}{R_1 n^4}(n^2-1) \tag{3.10}$$

   where t is the thickness of the gain medium, R is the curvature of the mir-

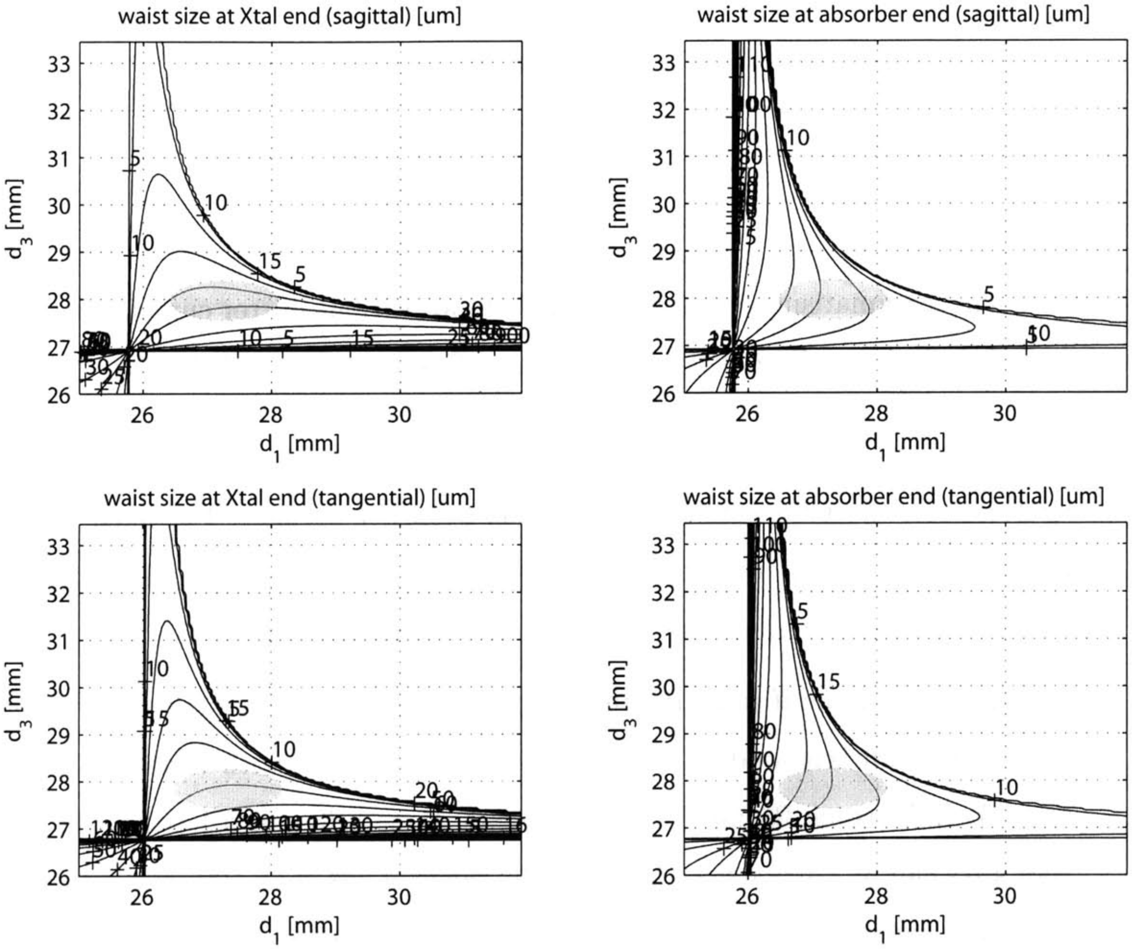

Figure 3-7: The stability diagram for 340MHz V-cavity configuration. R1=R2=50mm, $\theta_1 = 7.6°$, $\theta_2 = 4.0°$

ror, and n is the refractive index of the gain medium. By putting numerical value t=2.0mm, $R1$=25∼100mm, and n=1.52, the compensation angle θ_1 can be found as in Table 3.2.

θ_2 should be as small as possible since it only adds another astigmatism. Although smaller θ_2 would be preferred if mechanically possible, it will be hard to align SBR such that it does not block the beam coming to the mirror R2 if θ_2 is too small. The actual θ_2 in the experiment was between 2° and 4°.

Now that all parameters have been defined by the above procedures, the cavity can be built according to the parameters R1, R2, d1, d2, d3, θ_1, and θ_2. A numerical example of deciding these parameters is shown based on the actual experimental setup.

1. The desired repetition rate is f_R=340MHz. The corresponding cavity length is 440mm according to Eqn. 3.7. Assuming that the curvatures of both of the two curved mirrors, R1 and R2 are recommended to be 50mm as a starting guess and errors. Then d1 and d3 are going to have values around 25mm. Then d2 can be estimated to be 390mm by plugging these values into Eqn. 3.8.
2. Set the target spot size at the gain medium as $w_0 = 25\mu$m and the necessary fluence for the absorber as $F_{min} = 300\mu\text{J/cm}^2$. Then using Eqn. 3.9, the target spot size at the absorber surface is given by $w_a = 40\mu$m with average intracavity power $\overline{P_{intra}}$=5W.
3. Build the stability diagram with variations on d1 and d3. Assuming R1=R2=50mm, $\theta_1 = 7.6°$, and $\theta_2 = 4.0°$, a stability diagram is plotted with 25.0mm≤d1≤32.0mm and 26.0mm≤d2≤33.5mm in Fig. 3-7. In the stability diagram, partial region roughly bounded by transparent ellipse would satisfy the spot size requirement.

   From the stability diagram, we could find a reasonable amount of stable region that gives spot sizes small enough to satisfy the minimum fluence F_{min}. Therefore the first trial of R1=R2=50mm can be accepted for building the experimental setup.

3.1.2 Setup

This subsection describes practical procedures to build the designed cavity.

Characterization of pump laser diode

An InGaAs semiconductor laser diode was used for pumping in the experiment. In order to establish the current-intensity curve, the fiber-coupled laser diode was con-

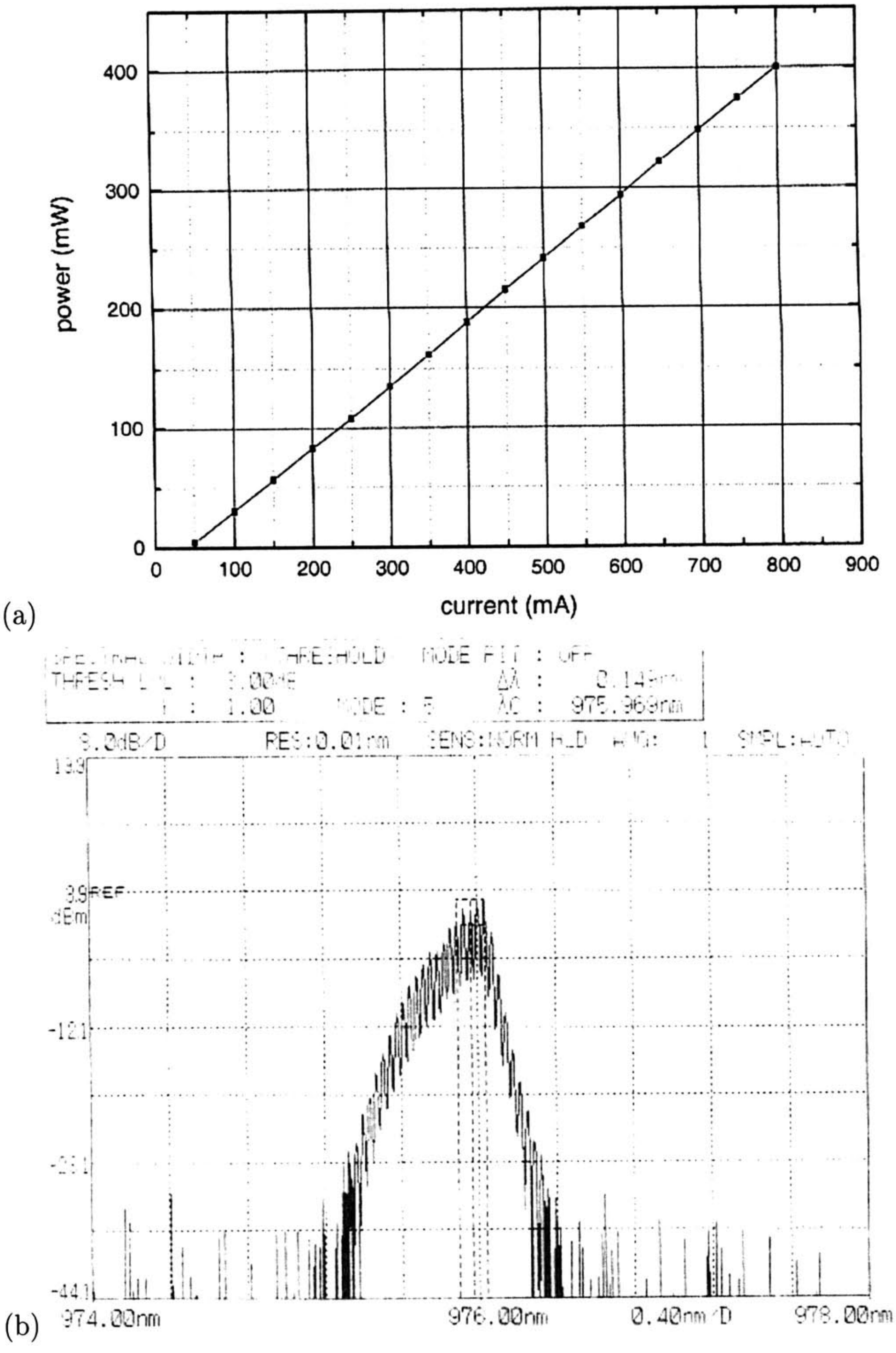

Figure 3-8: (a) Output power versus diode current for laser diode used for V-cavity configuration. (b) Optical spectrum of laser diode. Pump current was 97mA which corresponds to output power of 30mW.

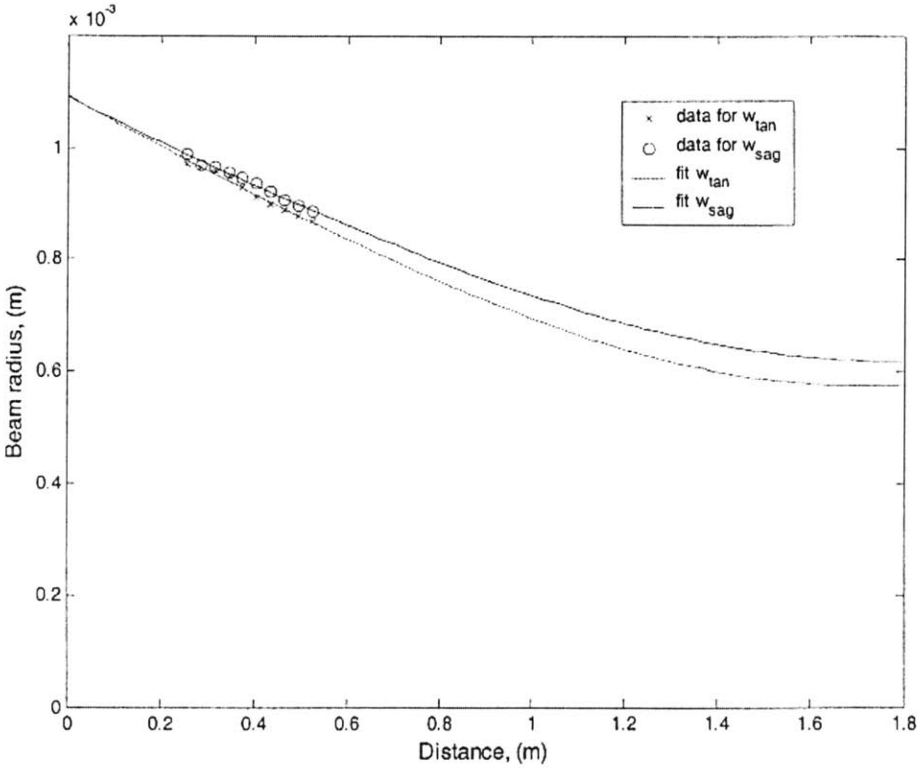

Figure 3-9: Beam profile of pump beam after collimator. Diode current was 150mA which corresponds to 57mW of output power.

nected to 980nm collimator and the output power was measured with power meter (Newport 1815-C). The measured curve is shown in Fig. 3-8(a). The threshold current I_{th} was 50mA and operating power was 0.4W at 800mA. The laser diode was packaged as a 14-pin butterfly type and mounted on the Thorlabs LM14S2 mount. The temperature of the diode was controlled to be constantly 20.00°C.

The optical spectrum of the laser diode was measured using Ando AQ-6317 optical spectrum analyzer. The measured data is shown in Fig. 3-8(b). The center wavelength was 976nm which was almost at the peak absorption wavelength 977nm.

The pump beam from the collimator is preferred to have as constant beam radius as possible while it propagates. Fig. 3-9 shows the beam profile of pump beam starting from the collimator. The beam radius measured at 10 points with 3cm interval for horizontal and vertical axis, and then the profile was fitted into gaussian profile along the distance from the collimator. Beam radii at tangential and sagittal

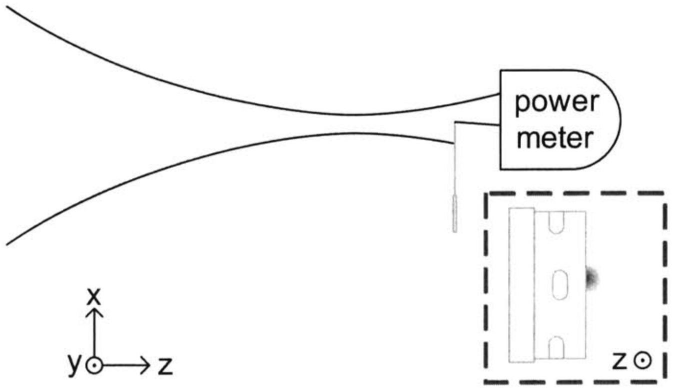

Figure 3-10: Knife-edge method to measure beam radius

focal plane were 575μm and 619μm, respectively. The beam radius at each position was measured using CCD camera (WinCamD$^{\text{TM}}$ from DataRay). If the beam radius were measured over broader range, we could obtain more precise spot sizes at the waist, but these waist sizes are considered to give us enough accuracy to design the pump optics.

Beam profiling

It is important to know how a beam profile looks like in a laser system since the beam size or intensity is critically connected to the performance of a laser. Two methods were adopted in this experiment for beam profiling.

CCD camera - Using a CCD (Charged Couple Device) camera to measure the beam radius at some position is a good and easy way to do. In addition to radius information, beam shape can be obtained, which makes it possible to figure out if the beam is single mode or not and further the M^2 value of the beam. However, in the following cases, different method should be applied instead of using camera:

- The wavelength of the beam to be profiled is out of the range that the camera supports.

- The beam radius is too big to fit in the camera sensor which is usually rectangle of a few millimeters at each side.

- The beam radius is too small for the camera to resolve. Usually if the beam radius goes under 100μm, it does not only become difficult to measure the beam radius, but the camera sensor may be burned by the intensity over damage threshold.

In the above cases, knife-edge method can be a substitute. Fig. 3-10 shows how the knife-edge method works for finding beam radius. Gaussian beam shape was assumed for this experiment. Assume that we want to measure the beam radius in x-direction. In that case, a knife is mounted such that its blade is parallel to y-direction. As the blade is slid into the beam along x-direction incrementally, the power of beam that passes the knife is measured using a power meter. The power versus distance in x-direction is fitted into erfc function using the least-mean-square approximation. Let the initial try of the center and the radius be x_z and w_z, respectively, and let the x-coordinate and the corresponding power be x_i and $P_i (i = 1, 2, ..., n)$. Then the sum of squared error for each measured data is

$$E_{spot}|_{x_j,w_j} = \sum_{i=1}^{n} \left(\frac{P_i}{P_{max}} - \text{erfc}\left(\frac{x_i - x_0}{\sqrt{2}w_0} \right) \right)^2, \tag{3.11}$$

where P_{max} is the maximum value out of $P_i (i = 1, 2, .., n)$. Then `fminsearch` function in MATLAB finds x_j and w_j that makes the error E_{spot} minimum.

After the beam radius is known at a position of z-axis, several more beam radii are measured at different z-coordinates. Let the z values and the corresponding beam radius be z_j and $w_j (j = 1, 2, ..., m)$. The beam profile is then fitted into a Gaussian beam propagation model. Let the initial try of the waist position and the spot radius be z_0 and w_0, respectively. The sum of squared error for each measured data is

$$E_{beam}|_{z_0,w_0} = \sum_{j=1}^{m} \left(w_j - w_0\sqrt{1 + \left(\frac{\lambda z_j}{\pi w_0^2} \right)} \right)^2, \tag{3.12}$$

where λ is the wavelength of beam to measure. Similarly to E_{spot}, z_0 and w_0 is found that minimize E_{beam}.

If the beam radius in y-direction needs to be measured, the blade is aligned along x-direction and similar procedures can be followed. According to above procedures,

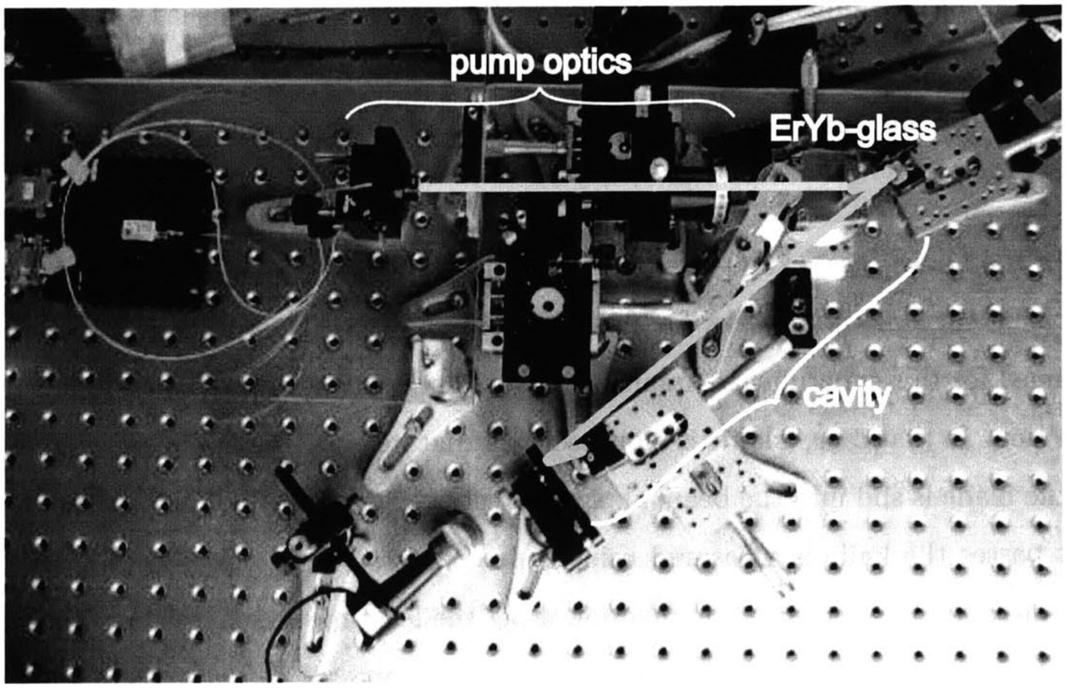

Figure 3-11: Picture of real setup for V-cavity configuration

a total of m×n power measurement is required to measure the beam waist size for each axis. It would be helpful to consider the resolution of the translational stage where the knife-edge is mounted, depending on the range of expected beam radius. For example, if the spot radius is around 10μm, the stage is recommended to be able to resolve at least 1μm.

MATLAB code for the above procedures is written in Appendix A, explaining how the fitting was implemented in detail.

Continuous wave operation

Pump optics

When we build pump optics, the following guidelines will be helpful for precise and stable alignment.

- The pump beam is strongly recommended to be parallel to one of the grid lines on the optical table. The parallelism helps the beam pass the center of lens such that aberration effect is minimized.

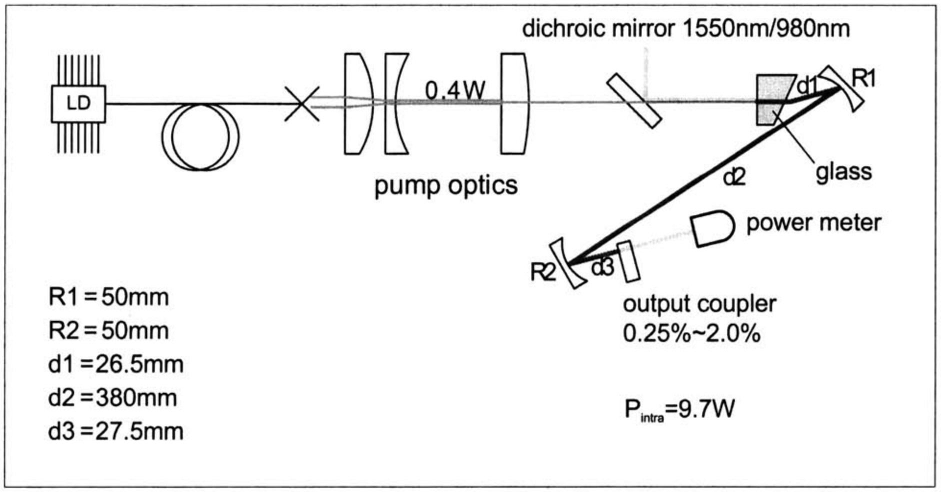

Figure 3-12: Measurement setup for V-cavity configuration laser operating in continuous-wave mode.

- The cylindrical lens can be tilted a little from exact perpendicularity to the beam axis to keep the pump beam from being reflected back into the collimator. The back reflection can potentially damage the pump laser diode.

- In order to make the pump beam pass the center of a lens, a camera or an iris can be utilized. With a camera, first the position of spot without the lens to be inserted is recorded. Then after putting the lens, it is aligned so that the spot on the camera remains at the same position. With an iris, the inserted lens can be adjusted so that the power after the iris maximized.

Actual setup

Fig. 3-11 shows the picture of the actual setup used for the V-cavity configuration. Pump optics, the glass mount, and the cavity are indicated. The beam height is set to 3.00". The larger the beam height, the easier it is to include additional degrees of freedom for each of the optical components. This should be done judiciously though, since increasing the beam height also increases the fundamental mechanical instability of the system. Therefore the beam height should be as small as possible while still allowing for the necessary degrees of freedom for adjustment.

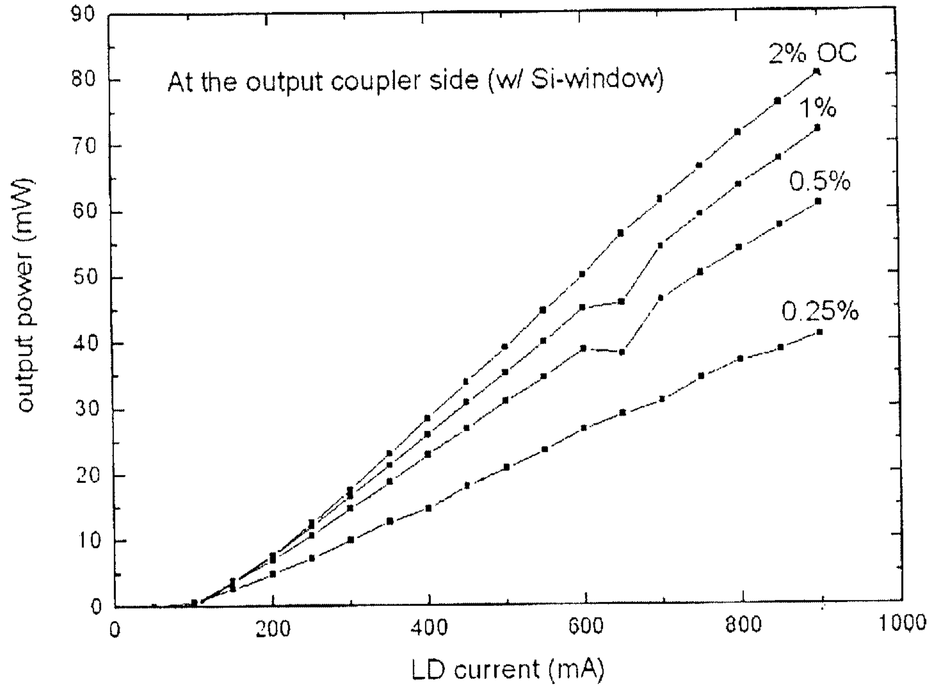

Figure 3-13: Output power versus pump power for various output coupling ratios (V-cavity)

3.1.3 Measurement setup and result

Continuous wave operation was first characterized before examining mode-locked operation. In the setup in Fig. 3-12, an output coupler was used instead of an SBR. We can optimize the cavity alignment by maximizing the intra cavity power of the laser operating at continuous wave mode.

Fig. 3-13 shows the output power versus the pump diode current for various output coupling ratios. As the output coupling ratio goes higher, the output power increased. The output power of 2% output coupling was almost two times larger than that of 0.25% output coupling. This also means that the intra-cavity power decreased as the output coupling ratio goes up. In case of 2% output coupling, we could obtain 80mW output power out of 0.4W pump power.

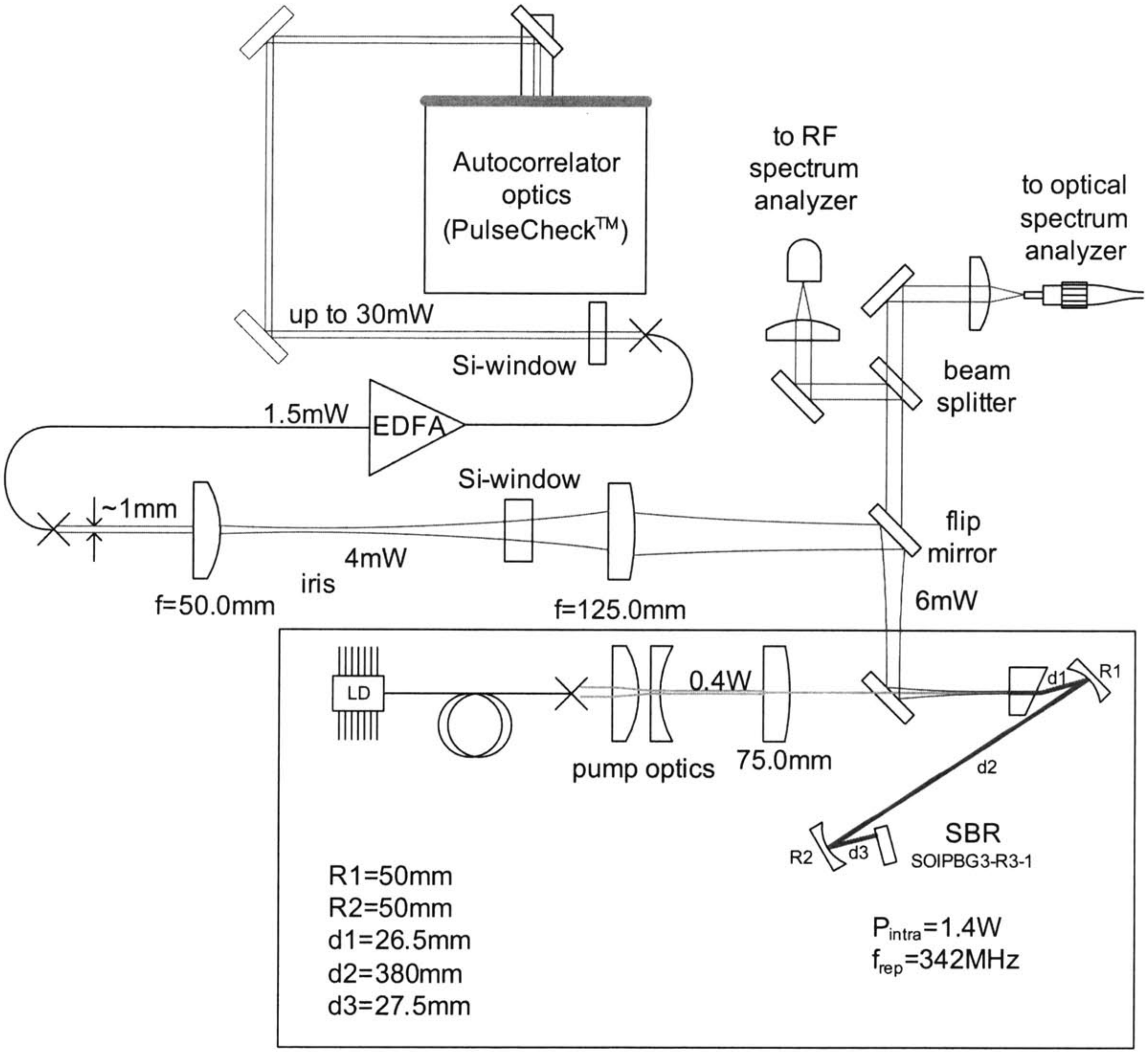

Figure 3-14: Measurement setup for V-cavity configuration laser operating mode-locked.

Mode-locked (pulsed) operation

To constitute a complete data set for the V-cavity configuration laser, the setup described in Fig. 3-14 was established. Three different measurements were conducted out of the mode-locked output laser beam: optical spectrum, radio frequency spectrum, and auto correlation to determine the pulse width.

- Optical spectrum

  To obtain the optical spectrum, the output beam was focused by 30mm convex lens and coupled into FC/PC connector which was connected to the optical spectrum analyzer (Ando AQ-6317).

- RF spectrum

  The RF spectrum could be measured using a fast photo-detector (ET-3000 from EOTech, 3GHz bandwidth) and a spectrum analyzer (HP8568B, 1.5GHz bandwidth).

- Auto correlation

  The output power from the mode locked laser was around 6mW. The output beam reflected at the flip mirror was collimated using two plano-convex lenses whose radius of curvature are 125.0mm and 50.0mm, respectively, since the output beam was diverging quite fast and beam path to the auto correlation setup could not be short enough to ignore the divergence. The collimated output beam has power of around 3mW which is not enough for the alignment and the auto correlation measurement. So the collimated beam is amplified using an EDFA (Erbium Doped Fiber Amplifier) up to 30mW. The auto correlation of the output pulse was measured using a commercial machine (PulseCheck^{TM}). One critical tip to align the beam for the auto correlator (AC) is that the beam hitting the mirror on the AC should be exactly parallel to the machine edge (indicated with a bold line on the AC in Fig. 3-14) and to the floor. Unless the parallelism is satisfied, it is very hard to see any pulse shape from the AC.

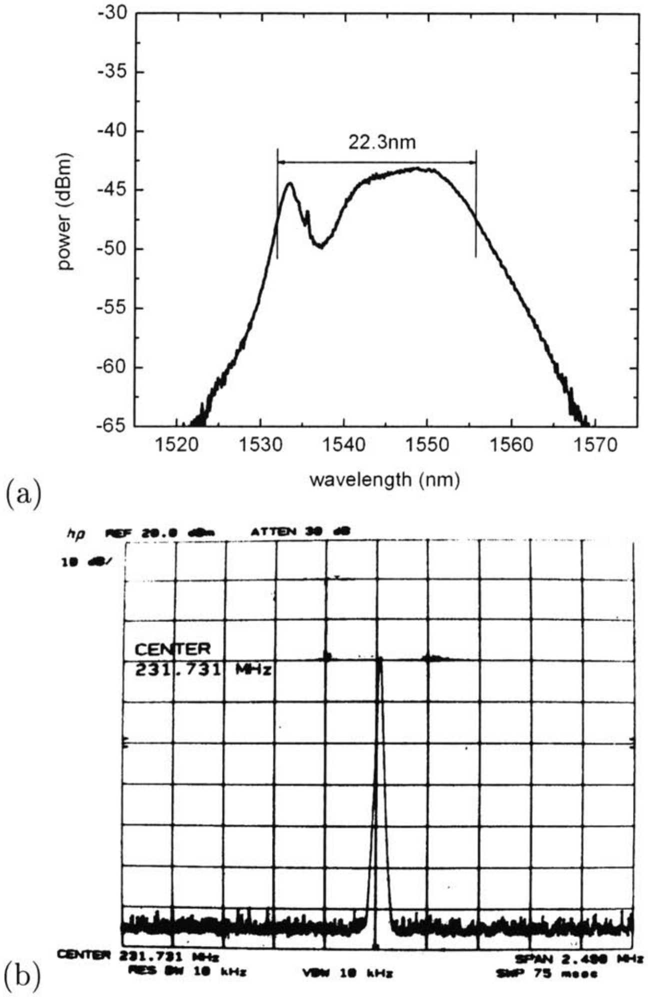

Figure 3-15: Measured data from 230MHz V-cavity laser. (a) Optical spectrum (b) RF spectrum

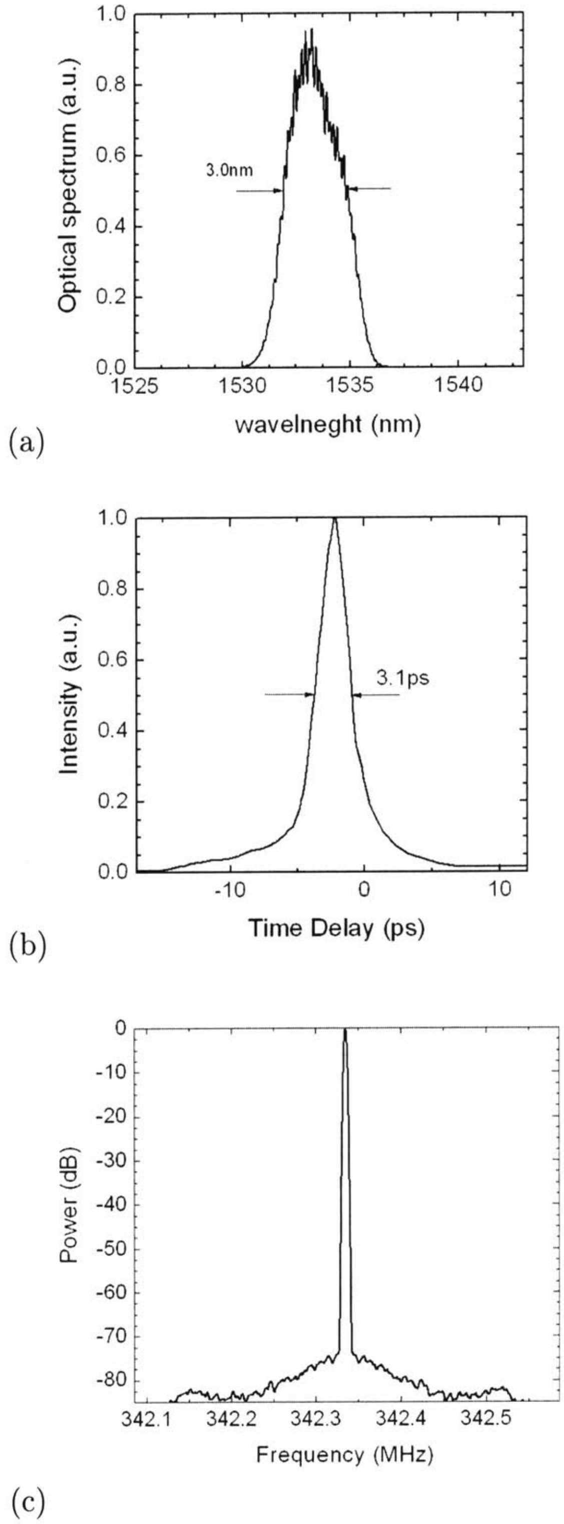

Figure 3-16: Measured data from 340MHz V-cavity laser. (a) Optical spectrum (b) Auto correlation (c) RF spectrum

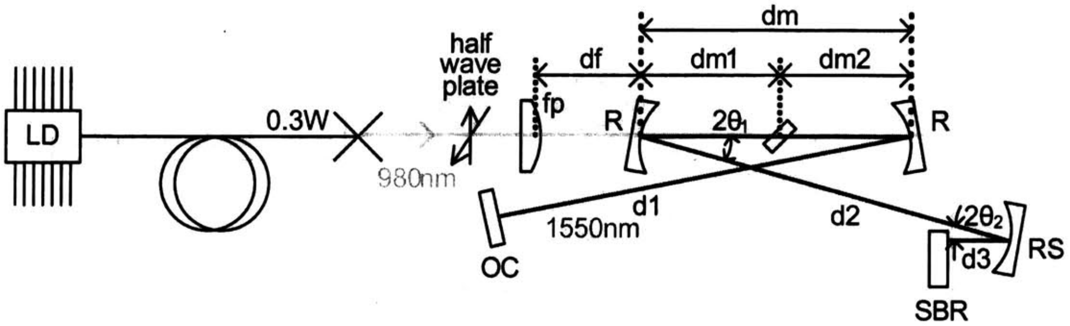

Figure 3-17: The schematic of Z-cavity configuration

Fig. 3-15 shows the measured data from the 230MHz V-cavity laser. The optical spectrum indicates that the bandwidth was 22.3nm which was almost twice as broad as that in [6]. This can be attributed to better pump optics where the distance between tangential focal plane and sagittal focal plane got smaller than before using a pair of cylindrical lenses instead of a pair of amorphous prisms. In the RF spectrum, the extinction ratio was over 65dB.

In the 230MHz cavity, a SiGe-SBR without resonant coating was used.

Fig. 3-16 shows the measured data from 340MHz V-cavity laser. In the 340MHz cavity, a SiGe-SBR with 3-layers of resonant coatings were used because the cavity was Q-switching with a non-coated SBR. The optical spectrum was 3nm, quite smaller than that of 230MHz cavity and the pulse width was 3.1ps, although the extinction ratio of the RF spectrum was over 70dB. This narrow bandwidth and broad pulse width may have been a result of spatial hole burning (SHB). In a V-cavity design, the gain is located at the end of cavity and experiences stronger spatial hole burning. This disallows the burned modes from being involved in mode-locking. [2, 9] Therefore another configuration of cavity where the gain medium is put in the middle of the cavity was explored in the following section.

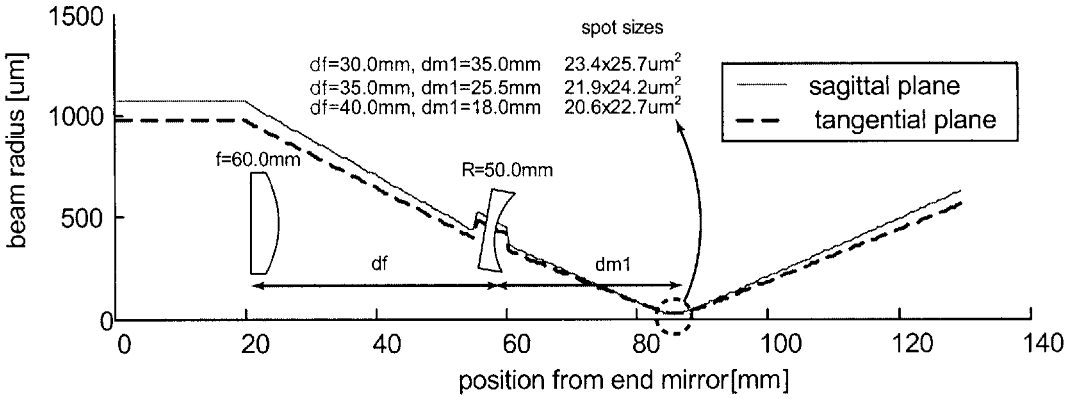

Figure 3-18: Beam profile of pump optics in the Z-cavity laser

3.2 Z-cavity

3.2.1 Design

The Z-cavity configuration features that the gain medium is located in the middle of cavity. Fig. 3-17 shows the schematic of Z-cavity configuration. 980nm pump with 0.3W power is supplied through a collimator and focused by lens fp. The half wave plate before the focusing lens changes the polarization of the pump beam such that the reflection at the gain medium is minimized. [2] The cavity is composed of three curved mirrors, the SBR, and one output coupler to tap the intra-cavity power.

Pump optics

The pump optics for the Z-cavity configuration laser is shown in Fig. 3-18. A plano-convex lens with the effective focal length of 60.0mm was used to focus the pump beam. The actual waist position formed a little farther than 60.0mm due to the diverging effect of the left curved mirror of the cavity. The spot size at the gain medium ranges from 20μm $\sim$ 25μm, depending on the distance from the focusing lens. The spot size was chosen to be similar to that of V-cavity configuration in Section 3.1.

---

[2] Only TM mode has Brewster's angle which minimizes the reflection.

Table 3.3: Parameters for the Z-cavity configuration and values used in this experiment

parameter	description and constraint	typical value in this experiment
R	The radius of curved mirror closer to the gain medium.	50mm
RS	The radius of curved mirror closer to the saturable absorber.	50mm
dm	The distance between right mirror R and left mirror R. dm ≅ dm1+dm2	$\sim$ R
dm1	The distance between gain medium and left mirror R	$\sim$ R/2
dm2	The distance between right mirror R and gain medium	$\sim$ R/2
d1	The distance between right mirror R and output coupler	200 - 400mm
d2	The distance between left mirror R and RS	$\sim 1.5 \times$ d1
d3	The distance between mirror RS and SBR	$\sim$ RS/2
θ_1	The incident angle in tangential plane at the left or right mirror R. Determined such that the astigmatism of the gain medium is compensated.	$5 - 10^\circ$
θ_2	The incident angle in tangential plane at the mirror RS. As small as possible. Generally limited by mechanical issue.	$2 - 5^\circ$

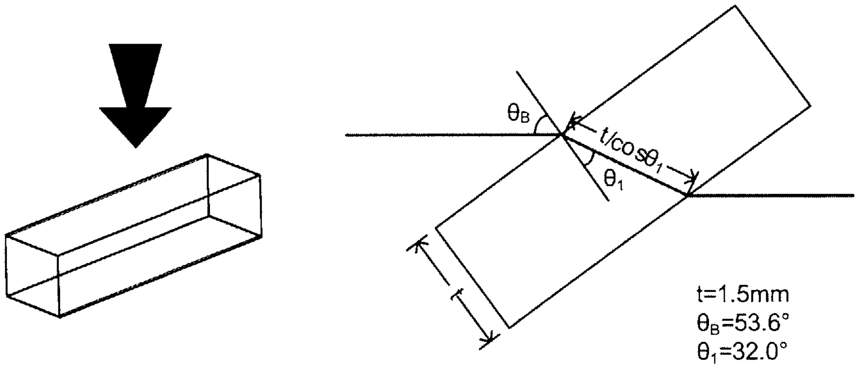

Figure 3-19: The dimension of ErYb-glass used as a gain medium for the Z-cavity laser.

Gain medium

The erbium-ytterbium doped glass used in the Z-cavity configuration was a rectangular parallelepiped from TwinStar Inc. Two facing polished surfaces are parallel to each other since the beam makes Brewster's angle on both of those surfaces. Fig. 3-20 shows the dimension and geometry of the glass piece. The physical length of gain medium along the beam path is 1.8mm when the glass is mounted at Brewster's angle.

Cavity dimension

Parameters that determine the dimension of the Z-cavity are listed in Table 3.2.1. We took the following procedures to decide the values of the parameters, similarly to the V-cavity case.

1. The desired repetition rate is f_R=230MHz. The corresponding cavity length is 650mm according to Eqn. 3.7. Assume that R and RS is recommended to be 50mm after several iterations and errors. Then dm=dm1+dm2$\simeq$R and d3$\simeq$RS/2. d1 and d2 can be estimated by

$$d1 + d2 \simeq L - (R + RS/2) \tag{3.13}$$

$$d2 = 1.5d1 \quad \text{(heuristic [19])} \tag{3.14}$$

   to be 230mm and 345mm, respectively.

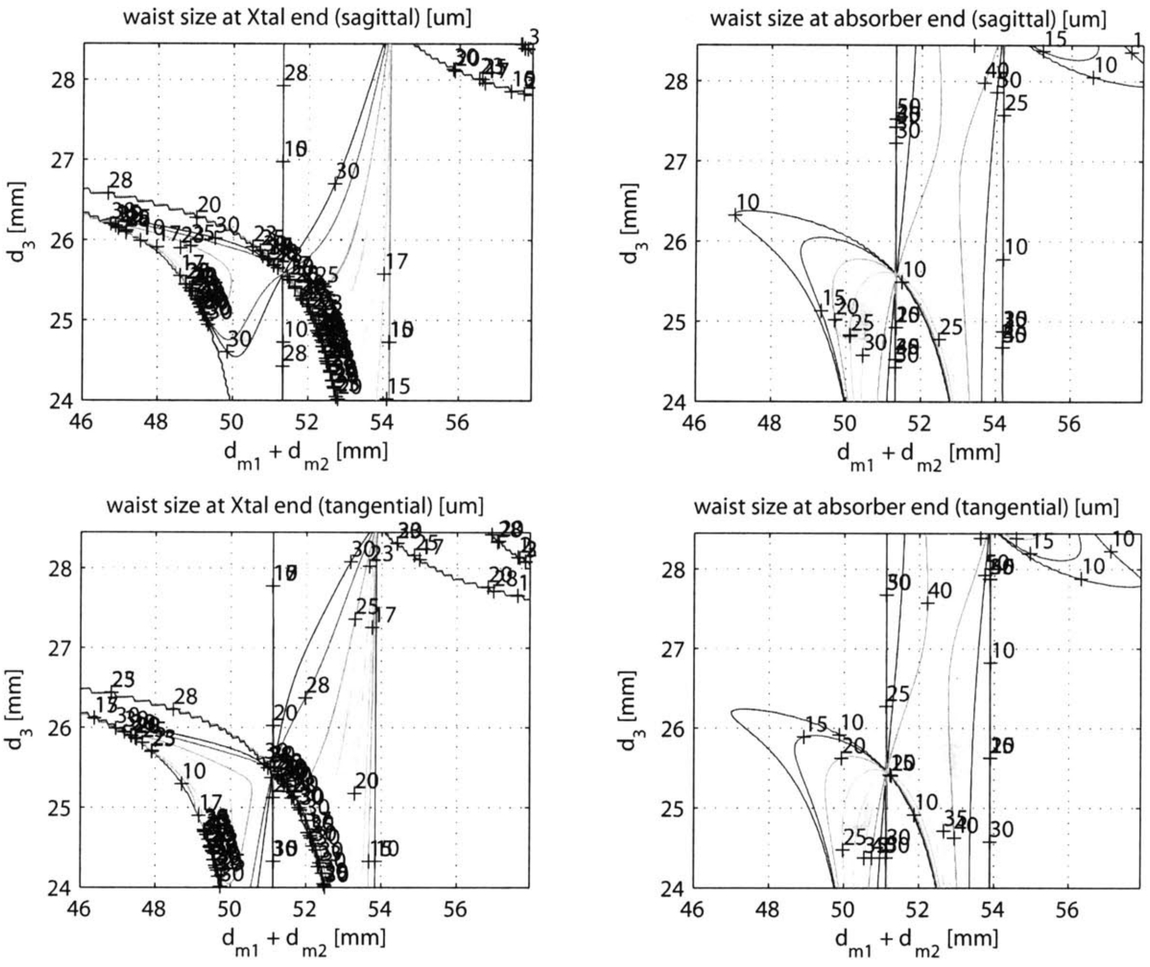

Figure 3-20: The stability diagram for 250MHz Z-cavity configuration. R=Rs=50mm, $\theta_1 = 7.3°$, $\theta_2 = 4.0°$, d1=250mm, d2=350mm

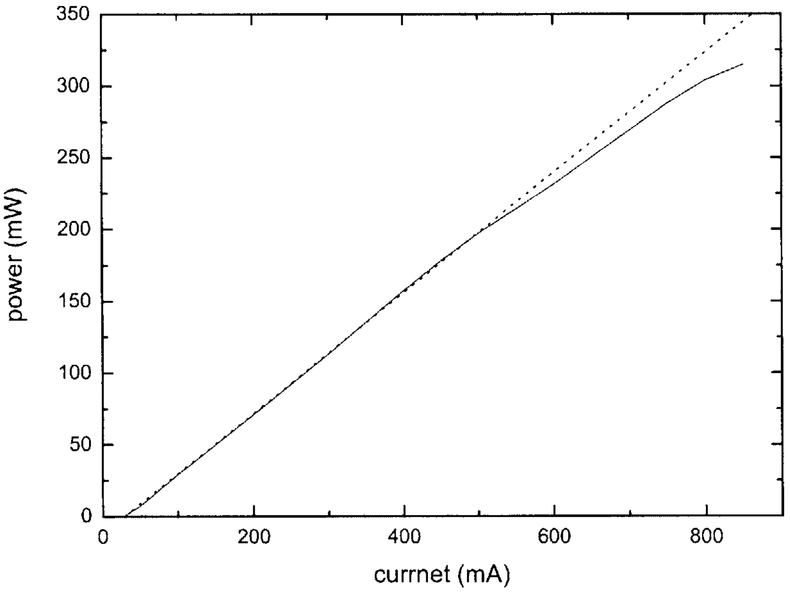

(a)

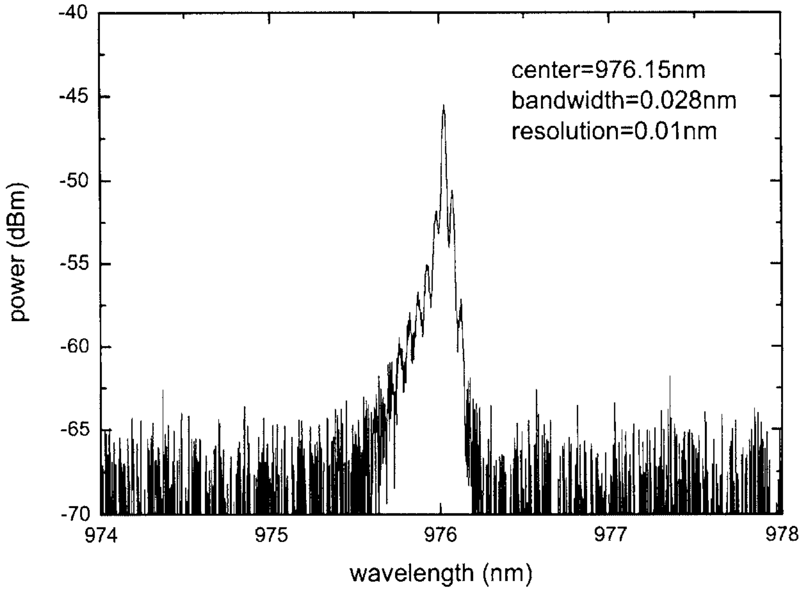

(b)

Figure 3-21: (a) Output power versus diode current for laser diode used for Z-cavity configuration. (b) Optical spectrum of laser diode. Pump current was 97mA which corresponds to output power of 30mW.

R1(mm)	θ_1 (deg)
25	10.3
50	7.3
75	5.9
100	5.1

Table 3.4: The astigmatism compensation angle θ_1 for various mirror curvatures. The thickness of the gain medium is 1.8mm and the refractive index of it is 1.52.

2. Set the target spot size at the gain medium as $w_0 = 25\mu$m assuming same glass doping level as in the V-cavity case and the necessary fluence for the absorber as $F_{min} = 300\mu$J/cm^2. Then using Eqn. 3.9, the target spot size at the absorber surface is given by $w_a = 48\mu$m with average intracavity power $\overline{P_{intra}}$=5W.

3. For the angles, $\theta_1 = 7.3°$ (Table. 3.4) in order to compensate the astigmatism induced by the two curved mirrors near the gain. $\theta_2 = 4.0°$, minimized value while mechanically feasible with the given beam radius around the curved mirror RS.

4. Build the stability diagram with variations on dm(=dm1+dm2) and d3. Assuming R=RS=50mm, a stability diagram is plotted with 46.0mm$\leq$dm1+dm2$\leq$58.0mm and 24.0mm$\leq$d3$\leq$29.0mm in Fig. 3-20. In the stability diagram, partial region roughly bounded by transparent ellipse would satisfy the spot size requirement.

   From the stability diagram, we could find reasonable amount of stable region that gives spot sizes small enough. Therefore the first trial of R=RS=50mm can be accepted for the experimental setup.

3.2.2 Setup

Characterization of pump laser diode

Fig. 3-21(a) shows the measured current-intensity curve for the laser diode used for pumping in the experiment for Z-cavity. The threshold current I_{th} was 30mA and

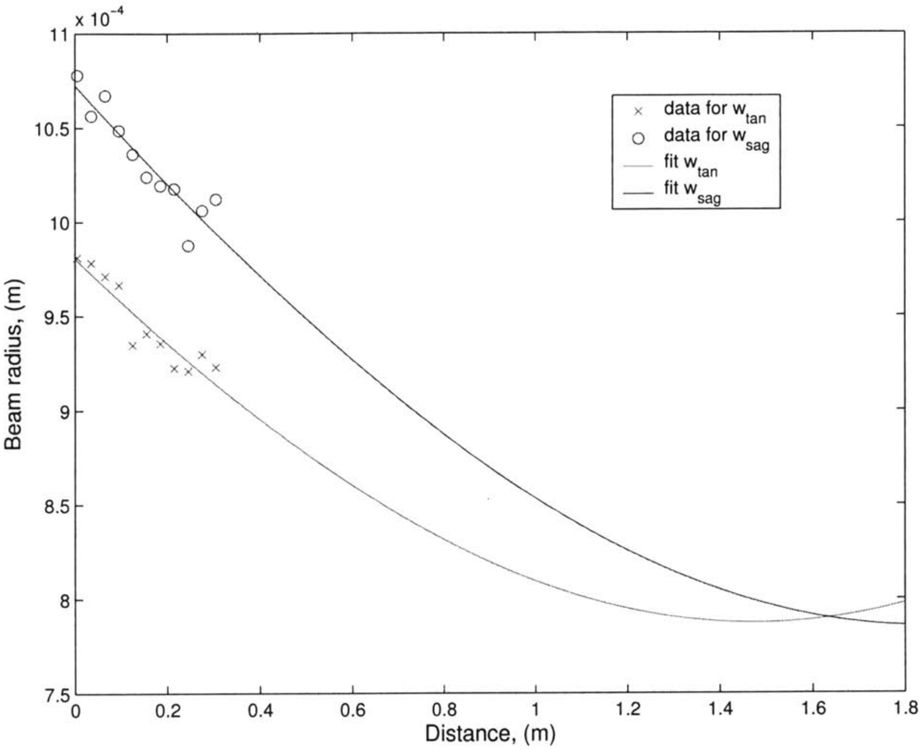

Figure 3-22: Beam profile of pump beam after collimator. Diode current was 50mA which corresponds to 7mW of output power.

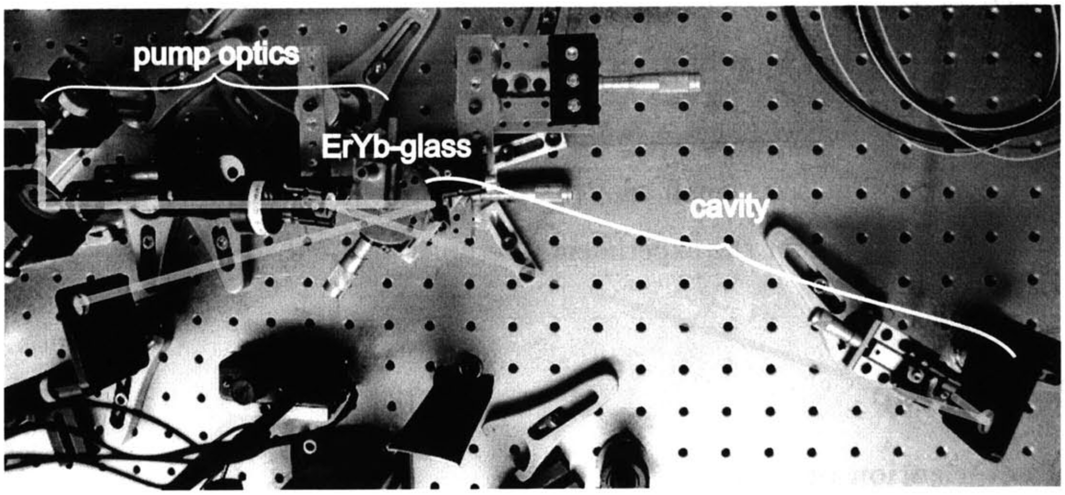

Figure 3-23: Picture of real setup for Z-cavity configuration

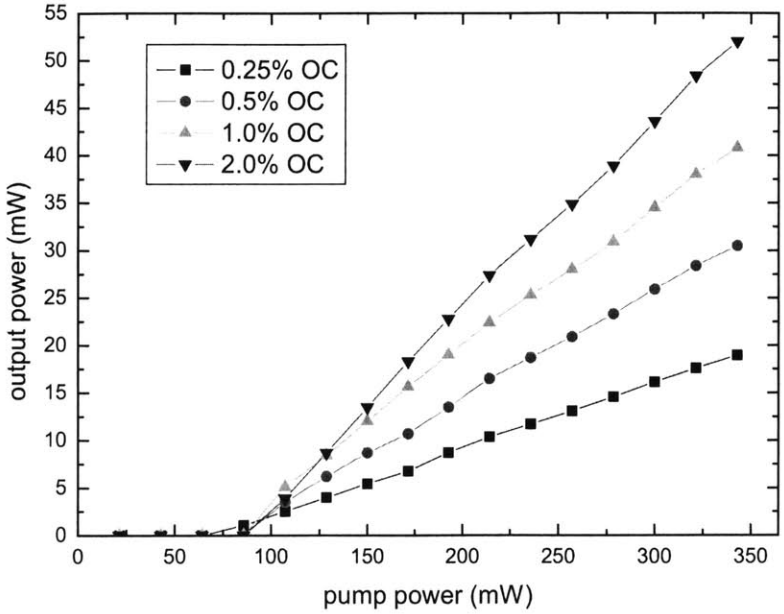

Figure 3-24: Output power versus pump power for various output coupling ratios (Z-cavity)

operating power was 0.3W at 800mA.

The measured optical spectrum of the laser diode is shown in Fig. 3-21(b). The center wavelength was 976nm.

Fig. 3-22 shows the beam profile of the pump beam starting from the collimator. The beam radius measured at 10 points with 3cm interval for horizontal and vertical axis, and then the profile was fitted into gaussian profile along the beam propagation path. Beam radii at focal plane were 787μm and 786μm for horizontal and vertical axis, respectively.

Real setup - picture

Fig. 3-23 shows the picture of real setup for the Z-cavity experiment. Pump optics, the glass mount, and the cavity are indicated. The beam height is set to 3.00". The entire setup without measurement part measures about 27" by 10".

3.2.3 Measurement result

Continuous wave operation was characterized in Fig. 3-24, which shows the output power versus the pump diode current for various output coupling ratios. For this data, an output coupler was used instead of an SBR. As the output coupling ratio goes higher, the output power increased. The output power from 2% output coupler was almost two and half times larger than that from 0.25% coupler. In case of 2% output coupling, we could obtain 50mW output power out of 0.3W pump power.

At the time of this writing, mode locking and further characterization of this arrangement is ongoing.

Chapter 4

Erbium-doped waveguides

An erbium-doped waveguide chip from Inplane Photonics Inc. (Fig. 4-1) is characterized for single pass gain (SPG), and the possibility of whether it can be used as a gain medium of a laser is examined.

4.1 Waveguide description

4.1.1 Fabrication

Er-doped waveguides are attractive candidates for the gain medium of an integrated mode-locked laser since erbium is compatible with the silicon fabrication processes. Several structures of planar optical waveguides doped with Er were reported [13, 21, 10, 23, 15]. The planar waveguide from [15] was made using RF sputtering and conventional lithography technology. Er^{3+}-doped films of aluminosilicate glass were RF-sputtered on an oxidized Si wafer and then waveguide cores were defined using conventional lithography. Finally standard silica cladding was deposited by LPCVD (Low Pressure Chemical Vapor Deposition).

The microscope image of the waveguide chip is shown in Fig. 4-2. The boundary of the chip measures 2cm by 2cm. In the lower part, several track-shaped waveguides are shown. Each track corresponds to a different length of the waveguide. In each length, bunch of four waveguides with different cross-sectional area are defined parallel. The

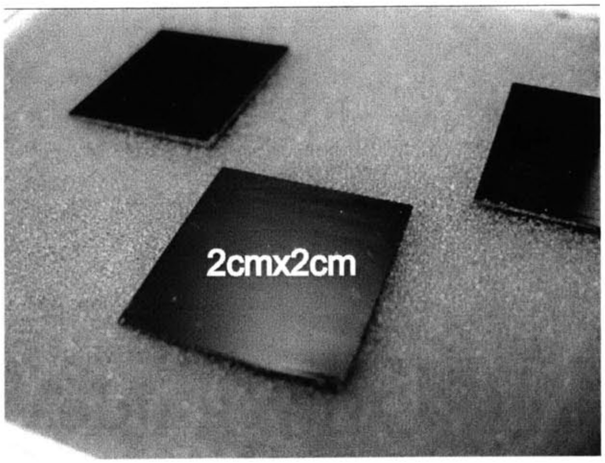

Figure 4-1: Photograph of the waveguide chip under test.

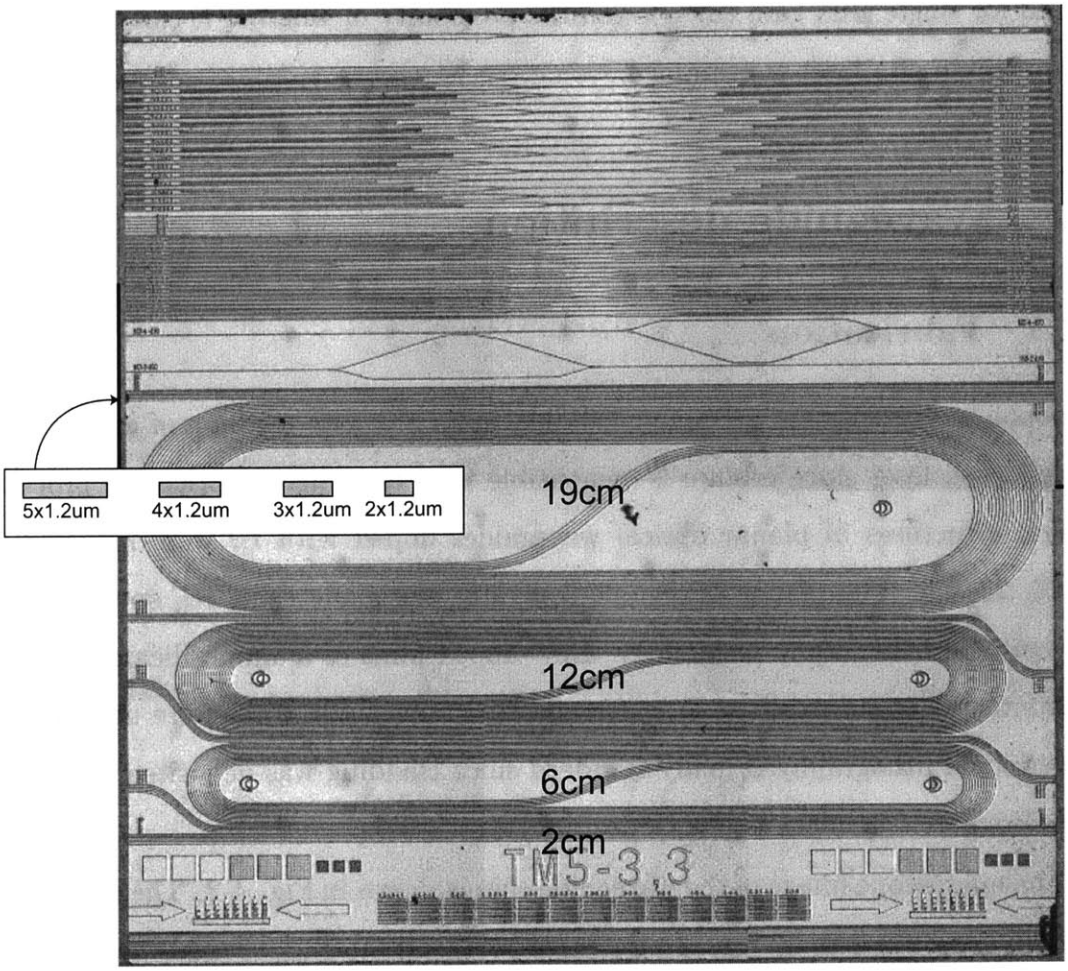

Figure 4-2: Microscope image of the waveguide chip under test. 2cmx2cm.

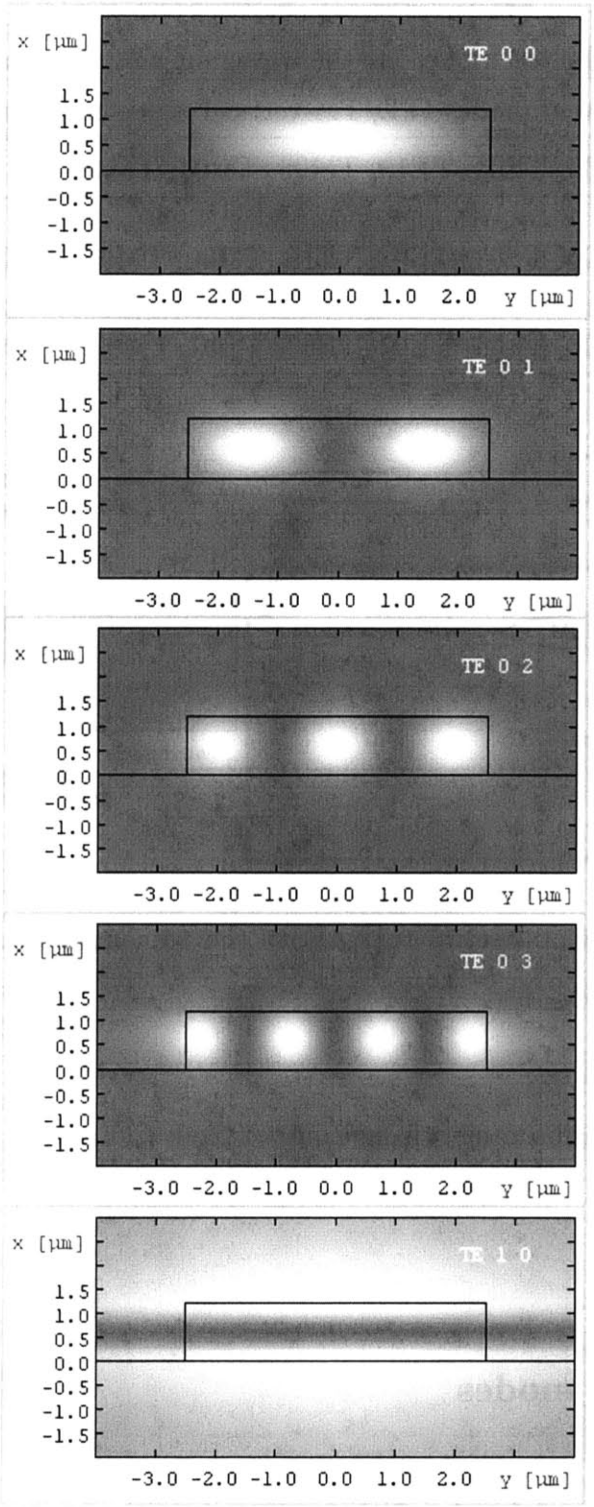

Figure 4-3: 2-D intensity profile of allowed modes in the 5μm × 1.2μm waveguide. Brighter parts have stronger intensity. Only TE modes are displayed here. TM00,01,... modes has same intensity profile as TE00,01,... modes shown in the above plots..

Table 4.1: Allowed modes for the waveguides of different dimensions

dimension	allowed modes (TE/TM-vertical order-horizontal order)
$2\mu m \times 1.2\mu m$	TE00, TE01, TE10, TM00, TM01, TM10
$3\mu m \times 1.2\mu m$	TE00, TE01, TE02, TE10, TM00, TM01, TM02, TM10
$4\mu m \times 1.2\mu m$	
$5\mu m \times 1.2\mu m$	TE00, TE01, TE02, TE03, TE10, TM00, TM01, TM02, TM03, TM10

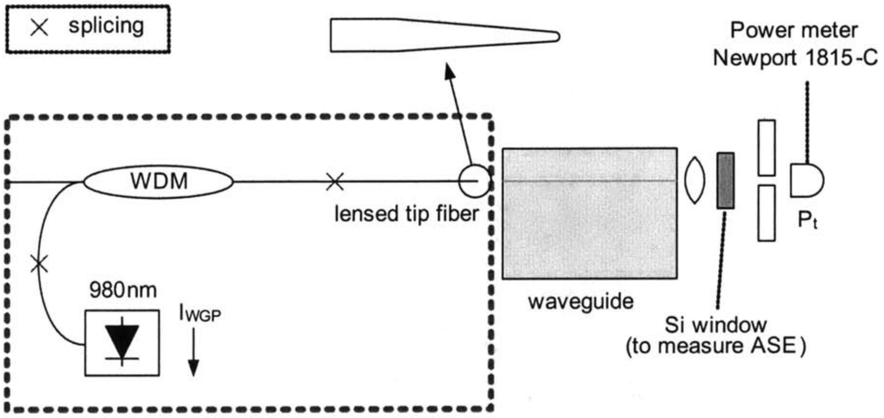

Figure 4-4: Experimental setup to measure the transmission and ASE (Amplified Spontaneous Emission) through the waveguides.

cross-sectional dimension ranges from $2\mu m \times 1.2\mu m$ to $5\mu m \times 1.2\mu m$.

4.1.2 Allowed modes

The waveguides were simulated to find the allowed modes using effective index method [1]. Four different dimensions were examined and the refractive indices of core and cladding were 1.6 and 1.45, respectively. Target wavelength was $1.55\mu m$. Table 4.1 shows the simulation result, the allowed modes for different dimensions. Intensity profile of each mode in case of the $5\mu m \times 1.2\mu m$ waveguide is shown in Fig. 4-3.

4.2 Measurement

4.2.1 Absorption

In this subsection, we measure how much pump beam is absorbed in the waveguides to excite the erbium ions.

Experiment setup

Fig. 4-4 illustrates the schematic of the experimental setup to measure the transmission or absorption of the waveguides. A fiber-coupled 980nm pump beam is connected to the lensed-tip fiber through a WDM (Wavelength Division Multiplexor) which is used in the next subsection for the measurement of single pass gain of the waveguides. The lensed-tip fiber from Nanonics Imaging Ltd. has 1.7μm spot diameter at the working distance of 4μm. It is mounted at the center of a fiber chuck [1] on a precision XYZ-stage of ±20nm resolution. The precision stage has three micrometer controls with ±1μm resolution and three piezo controls for each axis with ±20nm resolution. Using the stage, the lensed-tip fiber can be aligned exactly into the waveguides as small as 2μm by 1.2μm.

The pump beam coupled into the waveguides are mostly absorbed inside them. The pump beam passing through the waveguides are collected by an aspheric lens at the opposite side of the waveguide chip. The collected beam can go through an iris to block the beam that has been transmitted through the off-waveguide region. [2]

The power meter at the right end of Fig. 4-4 measures the power of the collected beam. The 980nm component indicates the power of the unabsorbed pump beam, while the 1550nm component filtered through a silicon window corresponds to the ASE (Amplified Spontaneous Emission). The silicon window used in this experiment had about 3dB loss at 1550nm and much more loss(absorption) around 980nm.

---

[1] The lensed-tip fiber should not have jacket in order to be clipped into a fiber chuck of 125μm gap. Trying to remove the jacket around the lensed-tip fiber is most likely to damage the fiber tip which is very fragile.

[2] Some part of the pump beam can be coupled into the cladding region.

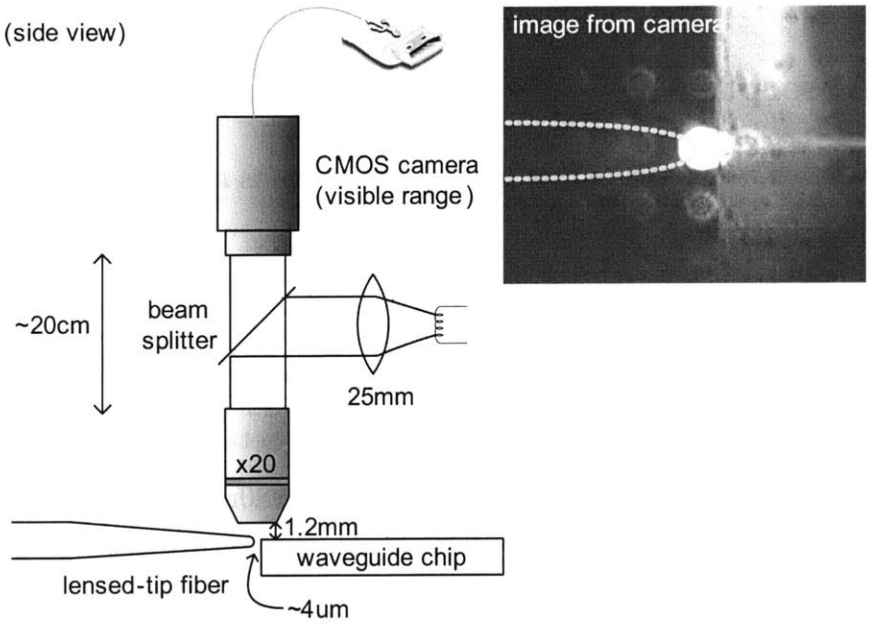

Figure 4-5: Setup for illuminating the lensed-tip fiber and the waveguide end for alignment.

Aligning the lensed-tip fiber into the waveguides needed not only a high precision XYZ-stage, but also an imaging system (Fig. 4-5) that makes the waveguide chip look bigger and shows which waveguide is being coupled with pump beam out of many waveguides. A microscope objective lens with a magnifying power of 20 was installed above the waveguide chip. A USB-interfaced CMOS camera displayed the magnified image into a 15" inch monitor. In order to have the image bright enough on the monitor, a parallel illumination was employed. Since the microscope objective lens shaded the waveguide chip with a working distance of 1.2mm, the illumination needed to be added using a beamsplitter between the camera and the lens. A low-cost halogen lamp was used as the light source and collimated with a 25mm plano-convex lens.

The inset of Fig. 4-5 shows an exemplary image observed from the camera. Yellow dashed line indicates the outline of the lensed-tip fiber. The center of the bright white dot overlaps the fiber tip. The array of white dots is guessed to be diffraction images from the lensed-tip fiber. The green line shows the fluorescence produced during the

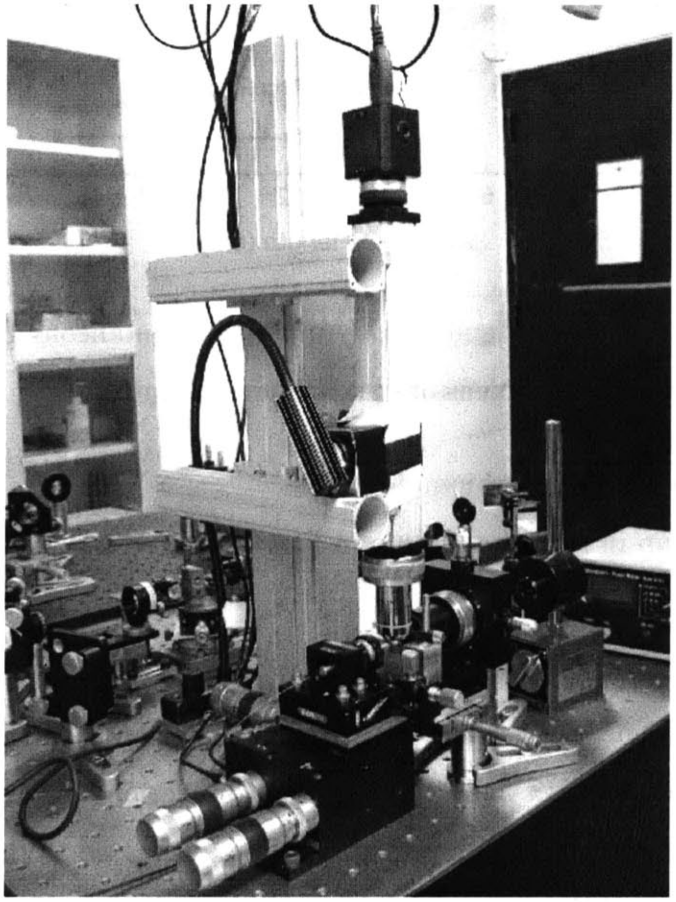

Figure 4-6: Lab setup for the waveguide chip characterization.

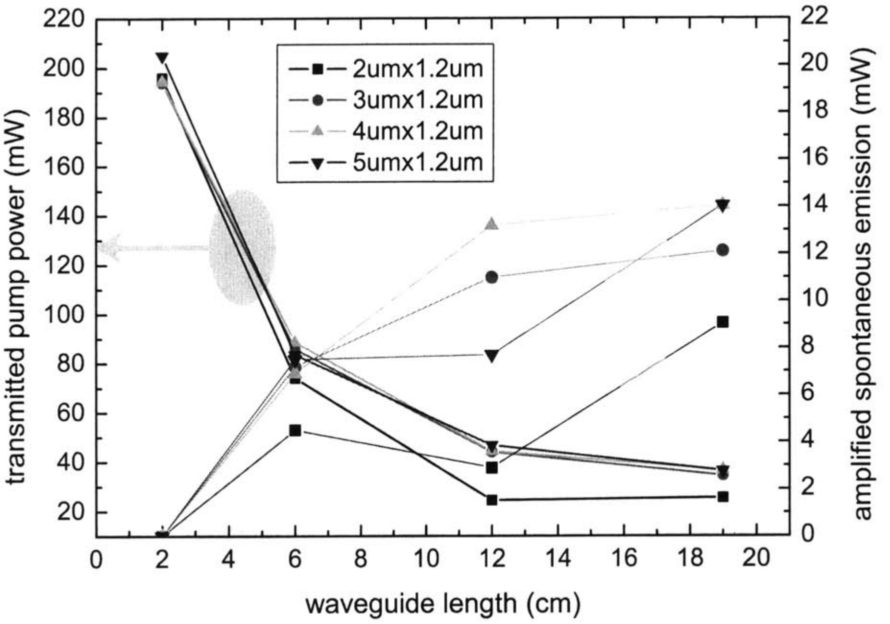

Figure 4-7: The transmission and ASE (Amplified Spontaneous Emission) through the waveguides of different dimensions and different lengths.

up-conversion process in the erbium doping.

The actual setup in the lab is shown in Fig. 4-6.

Result

Fig. 4-7 shows the measured transmitted pump power and ASE for sixteen combinations of waveguide length and cross-sectional dimension. As the waveguide gets longer, the transmitted pump power exponentially decreased. While 200mW pump power was transmitted through the 2cm waveguide, only 40mW passed through the 19cm waveguide. The transmitted power of 2μm-wide waveguide was a little lower than that of the waveguide of other widths. We guess that some specific modes of the pump beam was not allowed in the 2μm-wide waveguide while they were allowed in the wider waveguides. According to Table 4.1, those modes can be TE02 and/or TM02.

As for the ASE, longer waveguides gave larger ASE. Since longer waveguides absorbed more pump beam, they should have had higher inversion population, which leads to higher ASE intensity.

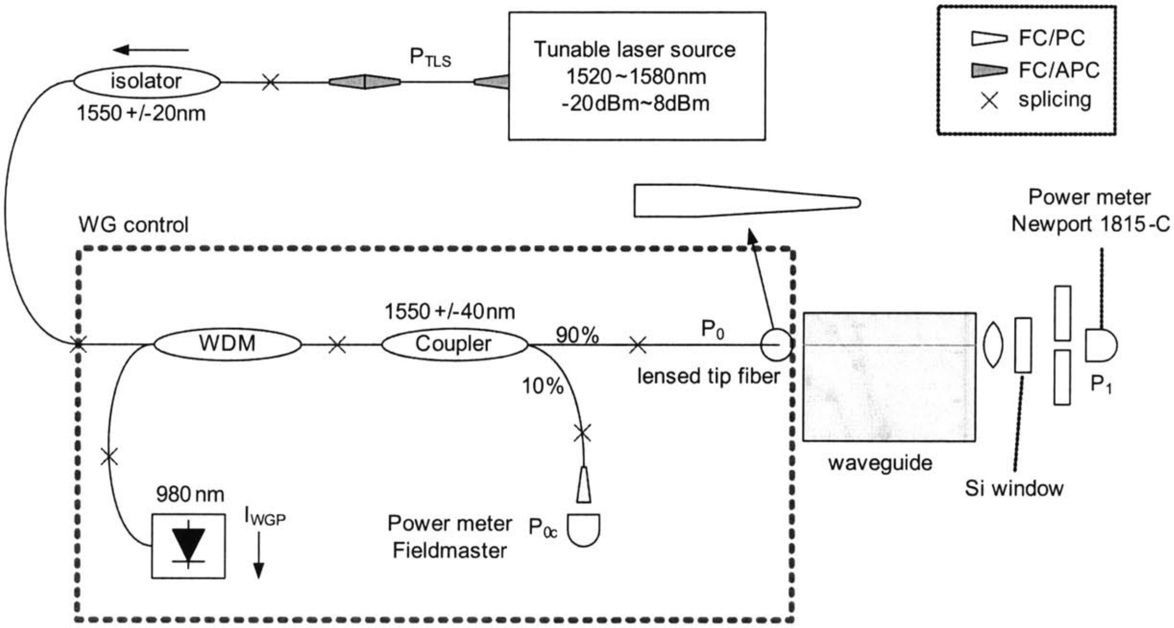

Figure 4-8: Experiment setup to measure the single pass gain of the waveguides.

4.2.2 Single pass gain

The single pass gain (SPG) of a gain medium is related to how much the incoming beam is amplified through the gain. When the output power after passing through the gain is equal to that of the incoming beam, the SPG is 0dB. In order that a gain medium can serve as a component of laser, the SPG of the gain medium should be larger than the total loss of the cavity.

Definition

The SPG G is defined as

$$G = 10\log_{10}\frac{P_1}{P_0}, \tag{4.1}$$

where P_0 is the input signal power in the lensed-tip fiber, and P_1 is the output power measured at the opposite side of the waveguides. P_0 is always larger than the power actually coupled into the waveguides due to the coupling loss. Thus this definition will make the calculated SPG smaller than the actual one by the coupling loss. However, since the coupling loss is hard to measure, coupling loss can be roughly estimated and added to the above calculated SPG. P_1 may also include the power of ASE, but

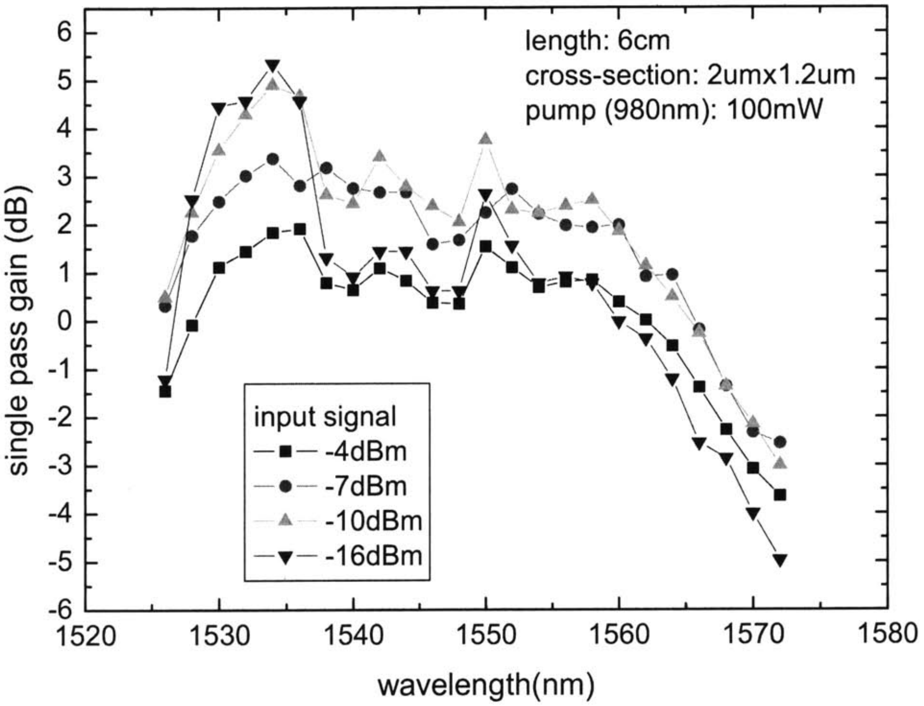

Figure 4-9: Single pass gain of the 6cm waveguide of 2.0μmx1.2μm cross-section versus wavelength for various input signal levels.

it is usually left uncorrected since the portion of ASE is quite small.

Experiment setup

The experimental setup to measure the SPG of the waveguides is illustrated in Fig. 4-8. A tunable laser source from Anritsu is multiplexed with 980nm pump beam using a WDM. The tunable source provides the signal input of 1530∼1570nm up to 6mW. In this experiment, an isolator was attached after the tunable source to prevent the back-reflected signal from screwing up the tunable source. 10% of the multiplexed light was tapped using a coupler to measure the P_0, signal power in the lensed-tip fiber. With the power P_{0c} at the 10% output of the coupler, the signal power would be $P_0 = 9P_{0c}$. Two things to note:

- The tapped power P_{0c} is recommended to be measured with the pump off. Small portion of the pump power can leak into the 10% port. This effect can be significant in case that the signal power is as low as the undesired pump power.
- The coupler should be put as close as possible to the lensed-tip fiber, such that the calculated input signal power P_0 includes fiber loss or splicing loss is as little as possible.

Result

Measured single pass gains for 6cm-long 2μm-wide waveguide are plotted in Fig. 4-9. With 100mW of pump power [3], the SPGs were evaluated for four different levels of input signal over 1530~1570nm. The plots tell us that the gain peak was obtained around 1535nm and the gain saturates as the input signal intenisty goes higher. The gain was about 5.5dB around the peak. However, the actual again will be over 10dB when we consider the 3dB loss of silicon window and the coupling loss >3dB between the lensed-tip fiber and the waveguide under measurement.

This experiment shows that the erbium-doped waveguide can be used as a gain medium of an on-chip laser.

---

[3] Measured at the output of the laser diode.

Chapter 5

Conclusions and Future Work

5.1 Conclusions

In this thesis, major components constituting on-chip mode-locked lasers were studied. In chapter 2, we addressed saturable Bragg mirrors which are compatible with silicon process to passively mode-lock lasers. As an effort to develop saturable absorbers for higher repetition rate lasers, resonant coatings were deposited on the previous SiGe saturable absorbers. New fabrication schemes were suggested and evaluated by simulations. In chapter 3, erbium-ytterbium glass bulk lasers were demonstrated as an apparatus to test the fabricated saturable absorbers. We addressed two kinds of cavity configurations and showed measurement results up to 340MHz repetition rate. Experimental techniques or tips were also mentioned to facilitate building the bulk laser setups. In chapter 4, erbium-doped waveguide chips from Inplane Photonics were characterized to show that it has gain high enough as the gain medium of on-chip integrated lasers.

5.2 Future work

Now that the erbium-doped waveguide from Inplane Photonics turned out to work as the gain medium of a laser, efforts to build waveguide lasers will follow. The next idea to be pursued is to put a coating on one side of the waveguide chip such that the

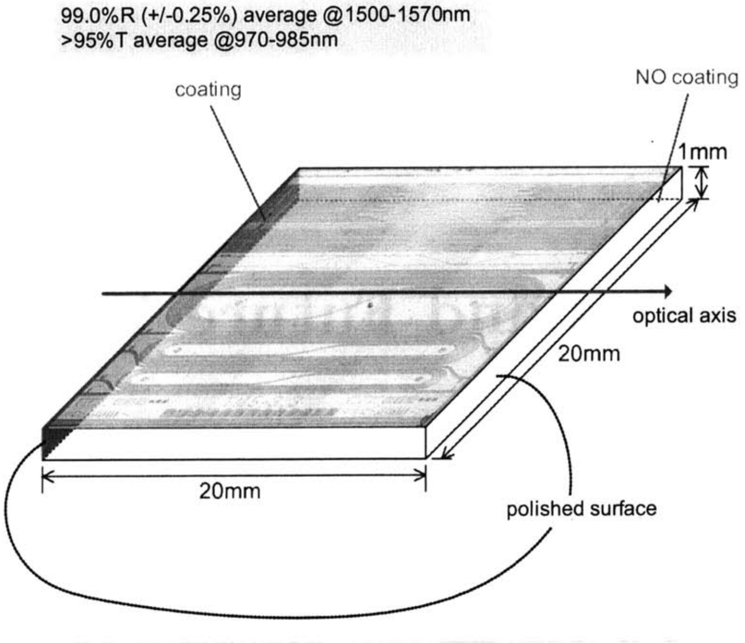

Figure 5-1: The waveguide can be coated on one side to build a waveguide laser.

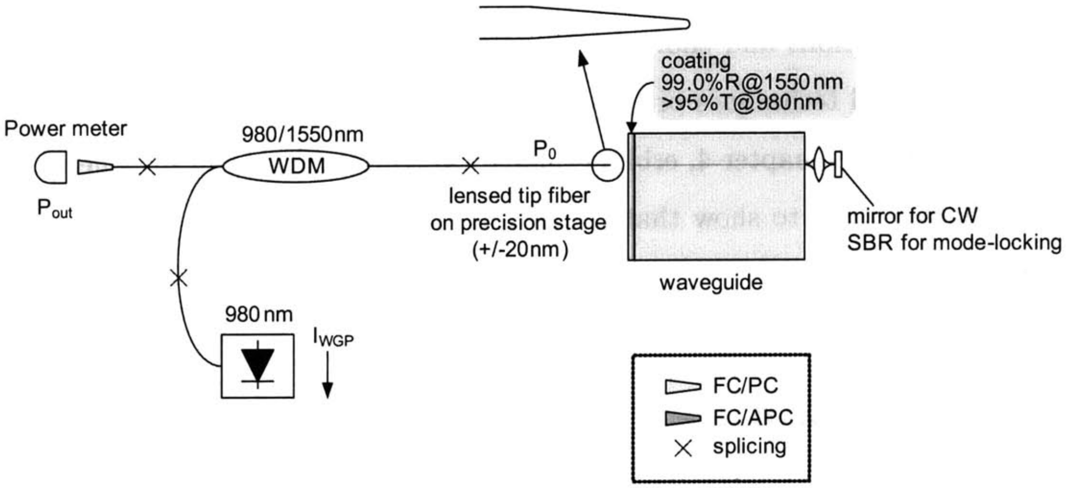

Figure 5-2: Schematic of waveguide laser setup

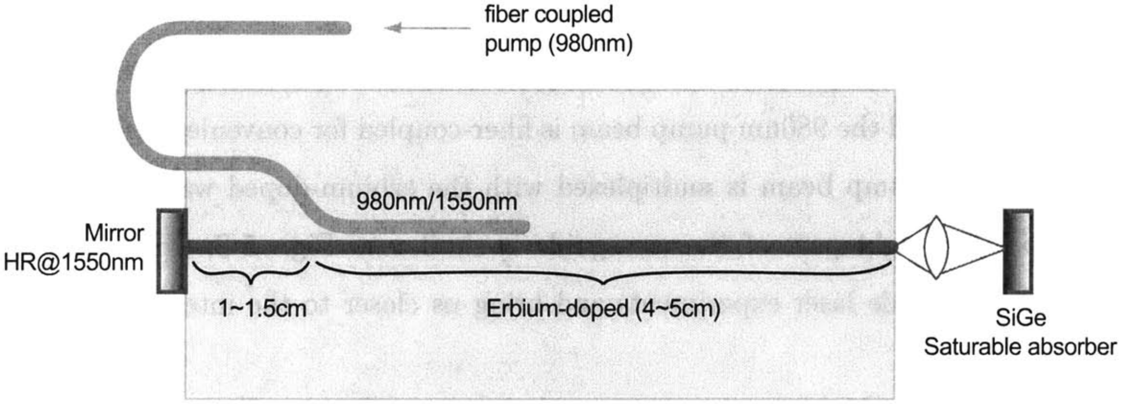

Figure 5-3: Schematic of next version of Er-doped planar waveguide from Inplane Photonics, Inc.

laser beam around 1550nm is mostly reflected and the pump beam around 980nm is mostly transmitted. (Fig. 5-1)

In the waveguide laser setup in Fig. 5-2, the coated waveguide chip replaces the original chip in the previous setup (Fig. 4-8). The coated side of the waveguide chip faces the lensed-tip fiber and the opposite side is open to the sequence of a focusing lens and an end mirror (or an SBR). The generated laser beam is coupled back to the lensed tip fiber through the coating on the waveguide chip by about 1%. The laser beam loaded into the fiber is separated from the fiber after passing the WDM and its power is measured. Expected challenges are as follows.

- Controlling the spot size of the laser beam at the right mirror or SBR due to the limited pool for lens selection. Butt-coupling the mirror or SBR to the waveguide can be considered as an alternative.

- Measuring the output laser power. Since the coupling loss is not known, it is hard to know the output power right after the waveguide chip before being coupled back into the fiber.

- Controlling the polarization of the pump beam. The waveguide allows only specific modes and polarization.

Inplane Photonics is going to provide next version of the waveguide chip. (Fig. 5-3) In the new chip, a coating similar to that in Fig. 5-1 will be put on one side of the waveguide and the 980nm pump beam is fiber-coupled for convenient and efficient pumping. The pump beam is multiplexed with the erbium-doped waveguide inside the chip. The right part of the waveguide is similar to Fig. 5-2. This chip will facilitate waveguide laser experiments and bring us closer to the integrated on-chip lasers.

Appendix A

MATLAB code for knife-edge measurement

```
clear all;
close all;

lambda = 980e-9; %wavelength in [m]
k      = 2*pi/lambda;

% *************** calculate waist sizes from measurements **********************
x1 = [20 100 110 120 130 140 150 160]*1e-6;
x2 = x1;
x3 = x1;
x4 = [-50 100 110 120 130 140 150 160]*1e-6;
x5 = x1;
x6 = x1;
x7 = x1;

% power measured with knife-edge method [arbitrary units]
power_x1 = [50.0 44.2 40.7 35.3 29.7 23.5 17.3 12.3];
power_x2 = [50.0 40.7 35.0 27.4 19.7 12.1  7.1  3.8];
power_x3 = [50.0 47.3 40.5 33.1 23.5 12.8  6.7  1.6];
power_x4 = [50.0 49.3 46.7 43.3 29.9 19.1  7.8  2.3];
power_x5 = [50.0 47.2 43.4 35.2 27.4 17.9 10.5  4.2];
power_x6 = [50.0 47.6 45.1 41.8 34.4 30.2 22.5 17.0];

% distances of point of measurement from laser [m]
dx       = [14 12 10 8 6 4]*1e-3;

% calculate beam position and waist
[x0_1, wx0_1] = KnifeedgeFit(x1, power_x1)
[x0_2, wx0_2] = KnifeedgeFit(x2, power_x2)
[x0_3, wx0_3] = KnifeedgeFit(x3, power_x3)
[x0_4, wx0_4] = KnifeedgeFit(x4, power_x4)
[x0_5, wx0_5] = KnifeedgeFit(x5, power_x5)
[x0_6, wx0_6] = KnifeedgeFit(x6, power_x6)


% ********** calculate Gaussian beam Parameters ***************
% **********        all units in [m]           ***************

% start-values for optimization
z0_est    = -0.010;
b0_est    = 0.005;
Param_est = [z0_est, b0_est];
wx        = [wx0_1 wx0_2 wx0_3 wx0_4 wx0_5 wx0_6];

%options for optimization algorithm
options=[]; %options=optimset('MaxFunEvals',10000,'Display','Iter');
```

```
xParam  = fminsearch('FitError_Gaussbeam', Param_est, options, dx,
wx, lambda);
% Calls FitError_Gaussbeam;
% Starts fitting with initial values specified in Param_Est
% no options specified
% d, w  : values for FitError_Gaussbeam
% lambda: additional parameter

z_x0 = xParam(1); b_x0 = xParam(2);

%calculate complex q-Parameters
q_x0=z_x0+j*b_x0

% calculate curves with estimated parameters:
dxmin=min([0, min(dx)]); dxmax=max([0, max(dx)]);
dx_calc=[dxmin:((dxmax-dxmin)/200):dxmax];
wx_calc=sqrt(2*b_x0/k*(1+((z_x0+dx_calc)./b_x0).^2));

% Plotting the data and calculated curves
figure; hold off;
plot(dx*1e3,wx*1e6,'bO'); hold on;
plot(dx_calc*1e3,wx_calc*1e6,'b');
legend('Data for wx','Fit for wx');
xlabel('Distance from laser [mm]','fontsize',11);
ylabel('Beam radius [um]','fontsize',11);
grid on;
```

```
function [x0, w0] = KnifeedgeFit(x, power)

% function [x0, w0] = KnifeedgeFit(x, power)
% x: readings from micrometer   power: corresponding power readings
% KnifeedgeFit calculates the waist size and position of the beam based on
% the data given in x and power.
% IMPORTANT: Assumes largest power levels at beginning of power-vector.
%            i.e. Start measurement with knife out of the beam, then drive it in.
%            (This gives a negative w0 value, if you want it the other way round,
%             use positive initial value for w0 !)

% normalize power levels
power   = power/max(power);

%start-values for optimization - may need to be changed
x0_est = 0.1;    % estimated position of center of waist in micrometer reading [mm]
w0_est = -0.1;  % estimated waist size [mm]
Param_est=[x0_est, w0_est];

%options for optimization algorithm
options=[]; %options=optimset('MaxFunEvals',10000,'Display','Iter');

% start fitting
Param = fminsearch('FitError_KnifeEdge', Param_est, options, x,
power);
% Calls FitError_KnifeEdge;
% Starts fitting with initial values specified in Param_Est
% no options specified
% x1, power1 -> values for FitError_KnifeEdge

% calculated parameters
x0 = Param(1);
w0 = -sqrt(2)*Param(2);  % error in previous version: must be multiplied bu sqrt(2) !!!

% calculate curves with estimated parameters:
xmin   = min(x);
xmax   = max(x);
x_calc = [xmin:((xmax-xmin)/200):xmax];
power_calc = gaussint(sqrt(2)*(x_calc-x0)/(-w0) );

% Plotting the data and calculated curves
figure; hold off;
plot(x, power, 'bx');
```

```
hold on;
plot(x_calc, power_calc,'b');
xlabel('micrometer reading [mm]', 'fontsize',11);
ylabel('normalized power, [a.u.]','fontsize',11);
```

```
function error = FitError_KnifeEdge(Param, x, power)
% function error = FitError_KnifeEdge(Param, x, power)
% calculates the error for fit of data in 'power' to specified 'x' positions

% values for use by algorithm
nopoi=length(x); err=0;

% extract start values form vector 'Param':
x0 = Param(1); w0 = Param(2);

% calculate error with lms
for m=[1:nopoi]
    err = err + ( GaussintForFit(x(m),x0,w0) - power(m) )^2;
end error=err;
```

```
function error=FitError_Gaussbeam(Param,d,w,lambda)
nopoi=length(d); err=0; z0=Param(1); b0=Param(2); for m=[1:nopoi]
    err=err+(BeamRadiusForFit(d(m),z0,b0,lambda)-w(m))^2;
end
error=err;
```

```
function w=BeamRadiusForFit(d,z0,b0,lambda) k=2*pi/lambda;
w=sqrt(2*b0/k*(1+((z0+d)/b0)^2));
```

```
function y = GaussintForFit(x, x0, w0)

% function y = GaussintForFit(x, x0, w0)
% returns normalized Gauss integral centered at x0 with width w0

y = gaussint( (x-x0)/w0 );
```

```
function y = gaussint(x) if (x<0)
    y = 1/2*erfc(-x);
else
    y = 1/2*(1+erf(x));
end;
```

Bibliography

[1] Effective index mode solver. http://wwwhome.math.utwente.nl/ hammer/eimsinout.html.

[2] F.X. Kärtner U. Keller B. Braun, K.J. Weingarten. Continuous-wave mode-locked solid-state lasers with enhanced spatial hole burning part i:experiments. *Applied Physics B:Lasers and Optics*, 61:429–437, 1995.

[3] Malvin Carl Teich Bahaa E.A. Saleh. *Fundamentals of Photonics*. Willey-interscience, 1991.

[4] H. Byun. Numerical modeling of the erbium-ytterbium glass micro-laser with repect to gain bandwidth and output power. *term paper*, 2005.

[5] F. Morier-Genound M. Moser C. Hoenninger, R. Paschotta and U. Keller. Q-switching stability limits of continuous-wave passive mode locking. *J. Opt. Soc. Am. B*, 16:46–56, 1999.

[6] F. O. Ilday H. M. Shen E. P. Ippen F. J. Grawert, J. T. Gopinath, J. Liu K. Wada F. X. Kärtner, S. Akiyama, and L. C. Kimerling. 220-fs erbium-ytterbium:glass laser mode locked by a broadband low-loss silicon germanium saturable absorber. *Optics Letters*, 30(3):329–331, 2005.

[7] J. T. Gopinath F. O. Ilday J. Liu H. Shen K. Wada L. C. Kimerling E. P. Ippen F. J. Grawert, S. Akiyama and F. X. Kärtner. Silicon-germanium saturable absorber mirrors. *Applied Physics Letter*, 74(26):3927 3929, 1999.

[8] Franz X. Kärtner Felix J. Grawert, F. Ömer Ilday. Analysis and active suppression of q-switching instabilities in mode-locked lasers - a control systems approach. *IEEE J. of Quantum*, 41(12):1518–1527, 2005.

[9] U. Keller F.X. Kärtner, B. Braun. Continuous-wave mode-locked solid-state lasers with enhanced spatial hole burning part ii:theory. *Applied Physics B:Lasers and Optics*, 61:569–579, 1995.

[10] N. Chiodo S. Taccheo G. Cerullo G. Della Valle, R. Osellame and P. Laporta. C-band waveguide amplifier produced by femtosecond laser writing. *Optics Express*, 13(16):5976–5982, 2005.

[11] Felix J. Grawert. *Stabilization Techniques and Silicon-Germanium Saturable Absorbers for High Repetition Rate Mode-Locked Lasers.* PhD thesis, MIT, September 2005.

[12] E. P. Ippen. Principles of passive mode locking. *Applied Physics B*, 58:159–170, 1994.

[13] J. Shmulovich A.J. Bruce R.K. Pattnaik J.-M. P. Delavaux, C. McIntosh and B.R. Wirstiuk. Gain flatness of a planar optical waveguide amplifier. *OFC*, 2000.

[14] H. Ebendorff-Heidepriem D. Ehrt R. Sauerbrey J.F. Philipps, T. Töpfer. Spectroscopic and lasing properties of er^{3+} : yb^{3+}doped fluoride phosphate glasses. *Applied Physics B*, 72:399–405, 2001.

[15] G.Lenz P.B.Hansen T.N.Nielsen D.J.Muehlner-G.A.Bogert I.Brener E.J.Laskowski A.Paunescu I.Ryazansky D.C.Jacobson J.Shmulovich, A.J.Bruce and A.E. White. Integrated planar waveguide amplifier with 15db net gain and 1550nm. *OFC*, 13(16):PD42–1 3, 1999.

[16] Franz X. Kärtner. 6.977 ultrafast optics. Lecture Note, spring 2005.

[17] U. Keller. *Semiconductors and Semimetals*, volume 59. Eds. San Diego, 1999.

[18] Ursula Keller. Recent developments in compact ultrafast lasers. *Nature*, 424:831–838, 2003.

[19] Jungwon Kim. Private communication.

[20] S. Taccheo P. Laporta, S. Longhi and O. Svelto. Analysis and modelling of the erbium-ytterbium glass laser. *Optics Communications*, 100:311–321, 1993.

[21] Casey F. Kane Miriam R.X. de Barros Gerald Nykolak Allan J. Bruce Ruby N. Ghosh, Joseph Shmulovich and Philippe C. Becker. 8-mw threshold er^{3+}-doped planar waveguide amplifer. *IEEE Photonics Technology Letters*, 8(4):518–520, 1996.

[22] J. Liu Student Member IEEE K. Wada G. K. Celler Member IEEE L. C. Kimerling Member IEEE S. Akiyama, F. J. Grawert and IEEE F. X. Kärtner, Senior Member. Fabrication of highly reflecting epitaxy-ready si.sio2 bragg reflectors. *Optics Letters*, 17(7):1456–1458, 2005.

[23] A. J. Faber Y. C. Yan, P. G. Kik H. de Waal, and A. Polman. Erbium-doped phosphate glass waveguide on silicon with 4.1 db/cm gain at 1.535 μ m. *Applied Physics Letter*, 71(20):2922–2924, 1997.